Vertical Profiles of Liquid Water Content in fog layers during the SOFOG3D experiment

Théophane Costabloz [1], Frédéric Burnet [1], Christine Lac [1], Pauline Martinet [1], Julien Delanoë [2], Susana Jorquera [2], and Maroua Fathalli [1]

[1]CNRM, Université de Toulouse,Météo-France, CNRS, Toulouse, France
[2]LATMOS/IPSL, UVSQ Université Paris-Saclay, Sorbonne Université, CNRS, Guyancourt, France

Correspondence: Théophane Costabloz (theophane.costabloz@meteo.fr)

Abstract.

A better understanding of the fog life cycle is required to improve forecasts by numerical weather prediction models and to reduce impacts of fog on human activities. However there are still many unknowns about the physical mechanisms driving fog variability. In particular, a main issue is that the transition from optically thin to thick fog is too sudden in numerical simulations. The liquid water content (LWC) profile is a key parameter, but observations in fog are sorely lacking. Here, we investigate observations from the SOuth west FOGs 3D experiment for processes study (SOFOG3D). In situ measurements collected under a tethered balloon provide 140 vertical profiles, which allow an exhaustive analysis of 8 thin fogs (thickness < 50 m) and 4 developed layers. We estimate the thin-to-thick transition period using thresholds for longwave radiation flux, turbulent kinetic energy, vertical temperature gradient, fog top height and liquid water path. In situ data are used to compute the equivalent fog adiabaticity from closure and compared with the value derived using a one-column conceptual model of adiabatic fog, assuming that LWC linearly increases with height. We found that the reverse trend of LWC profile (LWC maximal at the ground and decreasing with height) is ubiquitous in optically thin fogs under stable temperature conditions, while quasi-adiabatic features with increasing LWC values with height are mainly observed in well-mixed optically thick fogs under slightly unstable conditions. This study provides new insights into the evolution of LWC profile during the fog life cycle, to constrain numerical simulations.

1 Introduction

Fog is defined by the World Meteorological Organization as water droplets (sometimes ice crystals) in suspension in the atmosphere reducing the visibility at the Earth's surface below $1000 \, \mathrm{m}$ (5/8 mile) (World Meteorological Organization, 1956). This meteorological phenomenon affects human activities, and strongly perturbs the aviation, marine and land transportation, leading to human losses and high financial costs (Gultepe et al., 2007). Despite numerous studies on fog modelling, the accuracy

of fog predictions by numerical weather prediction (NWP) models remains a challenge (Müller et al., 2010; Steeneveld et al., 2015; Boutle et al., 2018; Westerhuis et al., 2020)

The difficulties encountered are related to low horizontal (Bergot and Guedalia, 1994; Pagowski et al., 2004; Boutle et al., 2016) and vertical resolutions (Beare and Macvean, 2004; Tardif, 2007; Edwards, 2009), surface heterogeneities (Bergot et al., 2015; Mazoyer et al., 2017), surface conditions (Duynkerke, 1999), large-scale conditions (Koračin et al., 2001), and initial conditions (Rémy and Bergot, 2009). Fog life cycle results from a complex interaction between radiative cooling, turbulence, microphysics, and non-local effects. Roach et al. (1976) and Teixeira (1999) illustrated the impact of radiative cooling for reliable fog predictions. The role of turbulence (Musson-Genon, 1987; Turton and Brown, 1987) and non-local effects related to complex terrain (Müller et al., 2010; Cuxart and Jiménez, 2012; Ducongé et al., 2020) were also evidenced.

In particular, a main issue concerns the transition from optically thin-to-thick fog being too sudden in numerical simulations and forecasts due to an excessive amount of liquid water in the fog layer (Poku et al., 2021; Boutle et al., 2022; Antoine et al., 2023). A fog becomes optically thick during its development phase when the layer closest to the ground radiates sufficiently in the longwave (LW) range to warm the surface below (Mason, 1982; Price, 2011). The downward LW radiation then increases so that the net LW flux becomes zero (Duynkerke, 1999; Wærsted et al., 2017; Dupont et al., 2016; Dhangar et al., 2021), while the fog optical thickness, which results from the contribution of geometric thickness and extinction also increases (Vehil et al., 1989). Its geometric thickness also increases (Wærsted et al., 2017; Price, 2011), as does the liquid water path (LWP) which results from the contributions of geometric thickness and liquid water content (LWC). As the fog top rises, it begins to cool by LW radiation, while the lower part of the fog is shielded from cooling and tends to warm. These two effects destabilise the temperature profile (Roach et al., 1976; Price, 2011) and the vertical temperature gradient becomes negative near the ground (Dupont et al., 2016). This destabilisation in turn creates small vertical motions within the fog layer which gives rise to turbulence (Nakanishi, 2000). However, this transition from thin-to-thick fog is not systematic, contrary to what fog simulations usually predict. Observations at Cardington (UK) and during the LANFEX campaign (Price et al., 2018) have shown that only 50% of sampled events become optically thick fogs (Price, 2011, 2019). Performing sensitivity tests on droplet concentration, Boutle et al. (2018) and Ducongé et al. (2020) found an optically thin-to-thick fog transition more consistent with observations. They suggested that a lower droplet concentration leads to greater droplet sedimentation, resulting in lower LWC values in the fog layer and thus optically thinner fog. Numerous studies have shown that aerosol properties and droplet size distribution representations through microphysical scheme are also a major cause of uncertainty in fog simulation and forecasting (Bott, 1991; Zhang et al., 2014; Stolaki et al., 2015; Maalick et al., 2016; Schwenkel and Maronga, 2019; Boutle et al., 2022; Fathalli et al., 2022). Therefore, observations of fog microphysics are essential to improve fog simulations.

Previous observations of ground-level microphysics have revealed large and rapid temporal variability of LWC in fogs (Gerber, 1981; Choularton et al., 1981; Fuzzi et al., 1984). Fog campaigns also highlighted significant differences in droplet size distribution during fog episodes (Kunkel, 1984; Wendish et al., 1998; Gultepe et al., 2009; Niu et al., 2011; Price, 2011; Mazoyer et al., 2019), among many others). Recently, Mazoyer et al. (2022) examined the evolution of microphysics during the fog life cycle and showed that it depends on the vertical development of the fog layer. However, most fog campaigns were carried out at ground level or on low masts, and observations inside the fog layer are rare due to the difficulty of the

measurements. The pionnering experiments of Okita (1962) along the slope of the Mt. Tokaschi (2070 m A.G.L) and Pinnick et al. (1978) with a tethered balloon, provided the first measurements of vertical profiles of microphysical properties in fog. More recently, Okuda et al. (2010); Egli et al. (2015); Price et al. (2015) have also reported microphysical measurements using a tethered balloon. Most of these measurements were conducted in deep well-mixed mature fogs, or fogs that lifted into stratus. In general, they revealed LWC profiles that were roughly constant or increasing with height, similar to aircraft measurements performed in stratus and stratocumulus clouds. Based on these observations and following the approach of Cermak and Bendix (2011), Toledo et al. (2021) have developed a one-column conceptual model of adiabatic continental fog by assuming that LWC linearly increases with height, but with a reduced condensation rate referred as the local adiabaticity. They used remote sensing data from 7 years of measurements performed at the SIRTA (Site Instrumental de Recherche par Télédétection Atmosphérique) observatory near Paris, to compute the equivalent adiabaticity by closure that would give the same LWP in the fog layer, but assuming a linear increase in LWC with height. They showed that this parameter is indeed positive for the majority of their data, corresponding to thick adiabatic and buoyant fog layers, but they noted some negative values for thinner fogs with LWP < 30 g.m^{-2}, suggesting that LWC could be higher at the surface and decrease with heigth in such cases. Using cloud radar reflectivity measurements, Wærsted et al. (2017) also retrieved higher LWC values near the ground for a thin fog event. Toledo et al. (2021) further proposed a parameterization of the equivalent adiabaticity as a function of cloud top height, producing negative values for thin fogs and converging to 0.65 for developed fogs.

Adiabaticity is a key parameter that describes the extent to which the actual liquid water amount in cloud deviates from the thermodynamically predicted adiabatic value. It has been extensively studied in shallow non precipitating clouds thanks to aircraft measurements (Brenguier et al., 2011; Wood, 2012; Braun et al., 2018), but in situ observations of the vertical profile of fog microphysics are sorely lacking in the literature. Addressing this issue in fog layers is important to evaluate fog life cycle prediction models and to better understand the physical mechanisms underlying the transition from thin to optically thick fog to improve numerical weather simulations.

The SOuth west FOGs 3D experiment for processes study (SOFOG3D) field campaign took place during winter 2019/2020 in the South-West of France to provide 3D mapping of the boundary layer during fog events (Burnet et al., 2020). The observation strategy combined vertical profiles derived from remote sensing instruments (microwave radiometer (MWR), Doppler cloud radar and Doppler lidars) and balloon-borne in situ measurements of fog microphysics and thermodynamics. Bell et al. (2022) and Vishwakarma et al. (2023) combined cloud radar reflectivity with temperature and humidity profiles and LWP retrieved from MWR, to better estimate the vertical profile of LWC in the fog layer. They demonstrated that LWC retrieval is highly sensitive to the prescribed droplet concentration, and that agreement with in situ data is highly dependent on cloud–fog heterogeneity. Dione et al. (2023) combined remote sensing measurements with the conceptual adiabatic fog model to analyze the thermodynamic and turbulent processes involved in fog formation, development and dissipation, focusing of the four deepest case studies : two radiation fogs and two advection-radiation fogs. They defined the different phases characterizing the fog's life cycle and provided quantitative analyses of key parameters and conditions that drive their temporal evolutions.

In this study, we examine in situ microphysical measurements collected under the tethered balloon during the SOFOG3D field campaign, to document the vertical profiles of LWC in the fog layer. For the first time, these observations provide an

exhaustive analysis of the evolution of vertical profiles of microphysical and thermodynamic properties during the fog life
cycle, from the formation phase in a thin stable layer to the well-mixed fog layer once vertical development has occurred, and
even during dissipation when fog lifted in a stratus cloud. They are used to investigate the actual fog adiabaticity in various
95   case studies and to compare it with the equivalent value proposed by Toledo et al. (2021).

This article is organized as follows, Section 2 describes the dataset and proposes an estimate of the thin-to-thick transition
period by considering a period of uncertainty using different thresholds. Section 3 introduces fog adiabaticity, presents the
methodology for analyzing the in situ data and compares these results with the equivalent adiabaticity values from closure and
based on a parameterization. Section 4 documents the evolution of LWC and temperature vertical profiles in the sampled fog
100   layers and provides new information for both thin and optically thick fogs. These results are discussed in section 5, followed
by the conclusion and outlook in section 6.

2   Dataset

2.1   Observational sites and instrumentation

The SOFOG3D experiment (Burnet et al., 2020) was conducted during the winter of 2019/2020 in the southwest of France in
105   the Landes forest region (Fig. 1a). A total of 17 instrumented sites were distributed over a 30 x 50 km area (red rectange in
Fig. 1). The Jachère site (44.41° N, 0.61° W) has been selected in a fallow field located in a large open area (Thornton et al.,
2023) and was specifically equipped for measurements of aerosols and fog microphysics as well as energy balance with in
situ instruments at the surface and on masts. The Charbonnière site, 1.4 km away over a flat terrain (Fig. 1b), was specifically
dedicated to remote sensing observations and tethered balloon operations. It was located close to an agricultural building for
110   convenience, and was open from SW to NE anticlockwise with a small forested area on the other side. Measurements from
these two sites are analysed in this paper to document the evolution of the vertical profile of the microphysical properties.

The instruments used in this study are summarized in Table 1. Both sites were equipped with a ground-based meteorological
station that provided standard dynamical and thermodynamical measurements such as temperature, wind speed and wind
direction as well as longwave and shortwave radiation.

115   A 95 GHz BASTA cloud radar was operated at the Charbonnière site on a vertical pointing mode. It measured radar reflec-
tivity and Doppler velocity up to 18 km with three vertical resolutions (12.5, 25, and 100 m) (Delanoë et al., 2016). The 12.5
m vertical resolution mode was dedicated to fog and low clouds, with the first available gate between 25 and 37.5 m a.g.l..
Cloud top height (CTH) was provided at a time resolution of 3 s, by the level 2 product developed by combining the three
modes to derive optimized radar reflectivity, velocity, and mask indicating the valid signal from noise. A additional mask was
120   defined to remove radar reflectivities when the tethered balloon was interfering with the cloud radar measurements (Delanoë,
2020). Since qualitative analysis of the BASTA reflectivities is performed here to provide geometrical thickness of the fog
layer, we choose to use all the available data and this specific mask is not applied. Cloud base height (CBH) was determined
using observations from a Vaisala CT25K 1/4 Hz ceilometer located at the Charbonnière site, measuring CBH for up to 3
cloud layers, with a vertical resolution of 15 m. An RPG HATPRO 1/10 Hz microwave radiometer (MWR) was also deployed
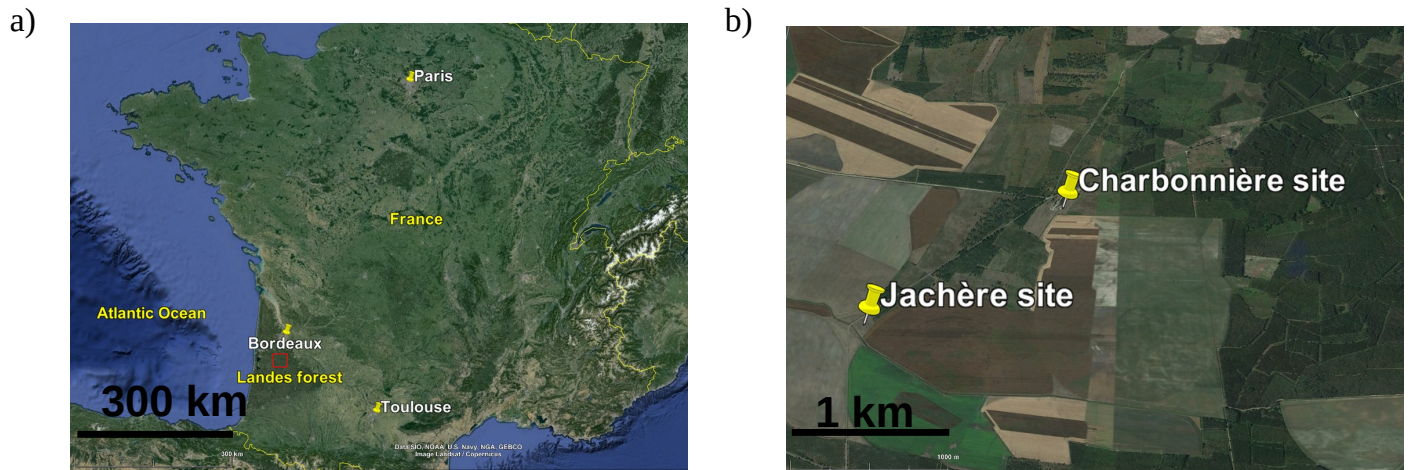
Figure 1. (a) Map of France with the location of SOFOG3D in red rectangle © Google Earth (b) Focus on the Jachère and Charbonnière sites © Google Earth.

at the Charbonnière site (Martinet et al., 2022). Using neural network inversion, it provided vertical temperature and humidity profiles up to 2.5 km with a vertical resolution of 25 m up to 100 m high and 30 m above, as well as the liquid water path (LWP) over the whole layer. The synergy between both instruments was investigated for IOP 11 (Vishwakarma et al., 2023) and IOP 14 (Bell et al., 2022), by combining the LWP retrieved from the radiometer and the reflectivity from the BASTA radar in order to better estimate the vertical profile of LWC within the fog layer. Here we analyze independently the BASTA radar and HATPRO radiometer measurements collected during 12 IOPs of the SOFOG3D experiment.

An 18 m^3 tethered balloon was operated at the Charbonnière site to provide in situ measurements through the boundary layer up to 500 m during the fog events. The payload consisted of an adapted DMT cloud droplet probe (CDP) for fog microphysics and meteorological sensors to provide thermodynamical vertical profiles of temperature, humidity, wind speed and wind direction. Depending on the period, a Vaisala tethersonde or a Gill ultrasonic anemometer and an inertial sensor were used for turbulence measurements (Canut et al., 2016), as indicated in Table 2. The CDP is an aircraft instrument that provides the size distribution of cloud droplets from 2 to 50 µm in diameter at 1 Hz (Lance et al., 2010). To operate under a tethered balloon, a wind vane was used to align the sampling section perpendicular to the wind, and a small fan fixed just to the rear of the laser beam sucked in the air flow. The air speed in the sampling section was therefore equal to the wind speed plus 5 m.s^{-1} (Fathalli et al., 2022).

2.2 Case studies

During the SOFOG3D campaign, 15 intensive observation periods (IOPs) with tethered balloon operations were conducted. Here we analyze 12 fog events sampled with the CDP under the balloon. Their charateristics are summarized in Table 2.

Table 1. List of instruments used in this study, references for uncertainty are : [1] (Delanoë et al., 2016), [2] (Martinet et al., 2022), [3] (Lance et al., 2010)

Instruments	Measured Variable	Unit	Vertical Position	Uncertainty	Temporal Resolution
PT100	Temperature	°C	2 m	0.5 °C	60 s
Young Wind Monitor	Wind Speed	$m.s^{-1}$	10 m	0.3 $m.s^{-1}$	60 s
	Wind Direction	°	10 m	3 °	60 s
Kipp and Sonnen Spectrometer	Downward/Upward Longwave Radiation	$W.m^{-2}$	1 m	10 %	60 s
METEK Sonic Anemometer	Turbulent Kinetic Energy (TKE)	$m^2.s^{-2}$	3 m	20 %	30 min
Young Visibility Sensor	Horizontal Visibility	m	3 m	10 %	60 s
Vaisala PWD22	Horizontal Visibility	m	3 m	15 %	15 s
BASTA Cloud radar	Reflectivity (Z)	dBZ		0.5-2 dBZ[1]	3 s
	Cloud Top Height (CTH)	m		12.5 m	3 s
CT25K Ceilometer	Cloud Base Height (CBH)	m		2 %	15 s
HATPRO Radiometer	Temperature	K		1.5 K RMSE[2]	10 min
	Liquid Water Path (LWP)	$g.m^{-2}$		20 $g.m^{-2}$	1 s
XSENS Sensor	Altitude (Z)	m		5 m	10 s
Rotronic Sensor	Temperature	°C		0.1 K	10 s
Gill Anemometer	Wind Speed	$m.s^{-1}$		1.5 %	10 s
Cloud Droplet Probe (CDP)	Liquid Water Content (LWC)	$g.m^{-3}$		30 %[3]	1 s
Vaisala RS41-SGP	Temperaure	°C		0.3 °C	1 s

The time of formation and dissipation, and the type of fog are determined on the basis of measurements at the Jachère site since visibility measurements at the Charbonnière site were only available between January 23, 2020 and March 4, 2020. A

145 fog event starts when visibilty falls below 1 km for at least 30 minutes, and dissipation occurs when visibility exceeds this threshold for more than one hour.

The algorithm developed by Tardif and Rasmussen (2007) was implemented to determine the type of fog that should reflect the main processes leading to fog formation. It depends on the magnitude of radiative cooling and wind speed, as well as the presence of precipitation or stratus cloud prior to fog formation. But threshold effects appeared for several cases leading to fog

150 being classified as either radiative or advective, even though these two major processes are equally important. This is because Tardif and Rasmussen (2007) considered radiative-advective fogs to be radiative fogs because no distinction was made between heating and air drainage. Given the importance of the advective component observed during SOFOG3D linked to the proximity of the Atlantic Ocean, we analyzed large scale conditions using synthetic analysis products, in addition to local conditions in the Supersite's surroundings at the fog formation, using satellite data, radar and thermodynamical parameters from meteorological

155 stations at the Jachère and Charbonnière sites. In particular, a sudden increase in longwave radiation, wind speed and specific

Table 2. Summary of the IOPs from the SOFOG3D campaign used in this study, based on the measurements at the Jachère site (except for the ending of the transition phase derived from the Charbonnière or Jachère site depending on the instrument). Types RAD and RAD-ADV correspond to radiation and radiation-advection fogs, respectively. Onset of the transition phase is based on Dione et al. (2023) for IOPs 11 and 14. The uncertainty on the transition phase duration, determined by the time interval between the first and last threshold of the transition ending (see text), is indicated in brackets. IOPs 13b, 14, 11 and 6c, will be studied more specifically in Section 4.

IOP	Date	Formation (UTC)/ Dissipation (UTC)	Duration	Type	Transition (UTC) Onset - [Ending interval] (duration)	Number of profiles : thin/thick/stratus - total
2a	05-06/12/2019	2139/ 0525	7h46	RAD		17/0/0 - 17
2b	06-07/12/2019	1924/ 0514	5h32	RAD-ADV		26/0/0 - 26
6a	03-04/01/2020	0141/ 0746	6h05	Precipitation		11/0/0 -11
6b	04-05/01/2020	2342/ 0121	1h31	RAD		3/0/0 - 3
6c	05-06/01/2020	2037/ 0928	12h51	RAD-ADV	NA - [2125-0130] (04h05)	0/24/2 - 26
9a	23-24/01/2020	2103/ 0138	4h35	Precipitation	2103 - [2104-2333] (2h29)	0/9/0 - 9
9b	24-25/01/2020	0040/ 0256	2h16	RAD		3/0/0 - 3
11	08-09/02/2020	2038/ 0349	7h11	RAD	2300 - [0030-0055] (0h25)	4/4/4 - 12
13a	22-23/02/2020	2303/ 0311	2h52	RAD-ADV		9/0/1 - 10
13b	23-24/02/2020	2104/ 0018	3h14	RAD-ADV		8/0/2 - 10
14	07-08/03/2020	2120/ 0705	8h31	RAD-ADV	2330 - [2342-0030] (0h48)	3/3/4 - 10
15	11-12/03/2020	2242/ 0417	5h35	RAD		3/0/0 - 3

humidity, as well as a decrease in visibility and variation in wind direction, reflecting advective processes, were analyzed for each case. This analysis enabled us to determine the most appropriate classification, allowing a fog to be classified as radiative-advective (Ryznar, 1977; Gultepe et al., 2007; Yang et al., 2018) if both aspects are considered significant. All other possible fog types were the same as those described by Tardif and Rasmussen (2007), i.e. radiative, advective, precipitation, stratus
160 lowering and evaporation fogs.

Three deep fog events with CTH higher than 200 m were sampled with the tethered balloon, namely IOP-6c, 11 and 14. Given such vertical development they have clearly undergone a transition from thin to thick. The life cycle of these cases has been examined by Dione et al. (2023) to analyze the thermodynamics and turbulent processes involved in fog formation, evolution and dissipation. Most of the fog layers sampled at the Charbonnière site, however, reached much lower thickness
165 than these 3 cases. Indeed we found only one additional thick fog on the database (IOP 9a), while the other 8 cases remained optically thin. For the 4 thick events, estimations of the onset and ending of the thin-to-thick transition are provided in Table 2 with a duration reflecting the associated uncertainty on the end of the transition based on a method described in the next section.

For the in situ measurements performed under the tethered balloon, the observation strategy consisted of ascents and descents through the layer to provide vertical profiles of the fog microphysics and thermodynamics, and constant-height sections at various altitude to investigate time evolution and turbulence within the fog layer. To be representative, the turbulent kinetic energy (TKE) is determined over constant-height sections lasting at least 20 minutes. Tethered balloon tracks for the four fog events analyzed in section 4 are illustrated in Fig. 8c, 9c, 10c and 11c superimposed to the radar reflectivity, for IOP 13b, 14, 11 and 6, respectively. The maximum ascent or descent speed of the balloon is 0.5 m.s^{-1}. It then theoretically takes 10 minutes to cross over up and down a 150 m-thick layer. However, due to the increase of the wind with the altitude that tends to sweep off the balloon away from the winch, the required time is much higher. In addition, the CDP is powered with a battery that allows measurements up to a maximum of around 1.5 hr. As a result, some profiles did not cross the entire fog layer from the ground up to the CTH and were discarded for this study. For 5 episodes, some vertical profiles were performed after the fog lifted into a stratus cloud during the dissipation phase, including the 2 thin cases sampled at the end of February. Overall a total of 140 vertical profiles has been selected, including 87 in thin fogs, 40 in thick fogs, and 13 in stratus clouds. The number of profiles is given for each IOP in the last column of Table 2. The number of profiles available in each phase of the life cycle is highly variable depending on fog duration, vertical extension and various technical difficulties encountered during operations. But with the exception of 3 events, there are between 9 and 26 profiles per fog case providing a unique dataset to document the vertical structure of the thermodynamics and microphysical properties of fog layers.

2.3 Determination of the thin-to-thick transition phase duration

As mentioned in section 1, a fog becomes optically thick when the layer closest to the ground radiates sufficiently in the longwave range to warm the surface below. This leads to the destabilization of the fog layer which evolves from a stable to a neutral or slightly unstable temperature profile. Precise estimation of the transition phase duration is not easy, however. Many authors have proposed various thresholds for different radiative, thermodynamic, geometric and microphysical parameters. We choose to define the onset of the transition phase on the basis of the Dione et al. (2023) study. The transition phase ending is determined by applying the following five conditions for the four thick fogs, in order to assess the uncertainty associated with the definition of the transition phase duration. This methodology allows us to evaluate whether multiple thresholds reached in a short period of time result in a rapid transition phase duration, and whether large discrepancies on the ending of the transition phase can be caused by local or non-local processes.

To smooth out high frequency fluctuations that are not representative of the typical length scale of the fog phases, we compute the transition duration ending for a given parameter from the 30-minutes running average of its time series except for TKE and vertical temperature gradient for which original sampling frequency data are used (Table 1).

– As the fog becomes optically thick, the longwave net radiation $LW_N = (LW_{DOWN} - LW_{UP})$ increases during the night and approaches 0 (Wærsted et al., 2017; Dupont et al., 2016; Dhangar et al., 2021). Mazoyer et al. (2017) observed a difference of 8 W.m^{-2} between LW_{DOWN} and LW_{UP} after the fog vertical development. We consider that the transition ends when $|LW_N| < 5$ W.m^{-2}.

- Warming at the surface and cooling at the fog top destabilize the vertical profile of temperature, which reverses from stable conditions and starts to decrease with height (Roach et al., 1976; Price, 2011). We use the temperature profile provided by the MWR just above the surface, but we have discarded the first two gates because of the excessive influence of the ground on the measurements. The considered threshold is when the temperature gradient between 50 m and 25 m becomes negative, i.e. $T_{50\mathrm{m}} < T_{25\mathrm{m}}$.

- Due to the destabilization of the vertical temperature profile, turbulent motions increase (Nakanishi, 2000). A threshold on σ_w^2 values is difficult to define. Price (2019) during the LANFEX campaign proposed σ_w^2 values higher than 0.002-0.005 $\mathrm{m}^2.\mathrm{s}^{-2}$ at the transition. But Dione et al. (2023) found much larger values ($0.01 < \sigma_w^2 < 0.04$ $\mathrm{m}^2.\mathrm{s}^{-2}$) during the stable/adiabatic transition of the 4 deepest fog events of SOFOG3D and an increase in TKE of up to 0.4 $\mathrm{m}^2.\mathrm{s}^{-2}$. These discrepancies may be explained by the contrasting environment between the two measurement areas, characterized respectively by a complex topography for LANFEX with sites located in valleys and at hilltops, and a relatively flat area at SOFOG3D with a mixture of open and forested sites (Thornton et al., 2023). In the same way, Dhangar et al. (2021), during the WIFEX campaign over New Delhi, considered a TKE threshold of 0.10 $\mathrm{m}^2.\mathrm{s}^{-2}$. We then choose TKE > 0.10 $\mathrm{m}^2.\mathrm{s}^{-2}$.

- An increase in geometrical thickness is systematically observed as the fog becomes optically thick. This vertical development can be detected using the fog cloud top height derived from cloud radars (Wærsted et al., 2017) or tethered balloon systems (Price, 2011). Based on theses studies we consider that the transition ends when CTH > 110 m.

- Finally, the LWP also increases. We apply the condition determined by Wærsted et al. (2017), i.e. LWP > 30 $\mathrm{g.m}^{-2}$.

The optical depth, τ, increases as the fog becomes optically thick (Vehil et al., 1989). Wærsted et al. (2017) consider opaque fog when $\tau > 5$. Droplet size distribution measurements from the CDP collected during vertical profiles provide the opportunity to compute the optical depth of the fog layer as :

$$\tau = \int_{Zb}^{Zt} \sigma_{ext}(z)dz \tag{1}$$

where σ_{ext} is the extinction, and Zb and Zt are the cloud base and cloud top heights, respectively. Optical depth from CDP measurements is computed for each of the 140 vertical profiles to provide an independent assessment of the optically thin and thick foggy periods.

Results for IOP 14 case study are illustrated in Fig. 2. Each transition ending time for a given parameter is represented by a vertical bar on the corresponding time series in Fig. 2b-f and they are all reported in Fig. 2h for a synthetic representation. Optical depth (Fig. 2g) reveals low values for the first 3 profiles with $\tau < 1$, while it remains close to or above the threshold of 5 from profile # 4. This suggests that fog becomes optically thick between 2315 (# 3) and 0049 UTC (# 4). These observations are consistent with Dione et al. (2023) who defined the onset of the transition phase at 2330 UTC. In addition, the transition phase
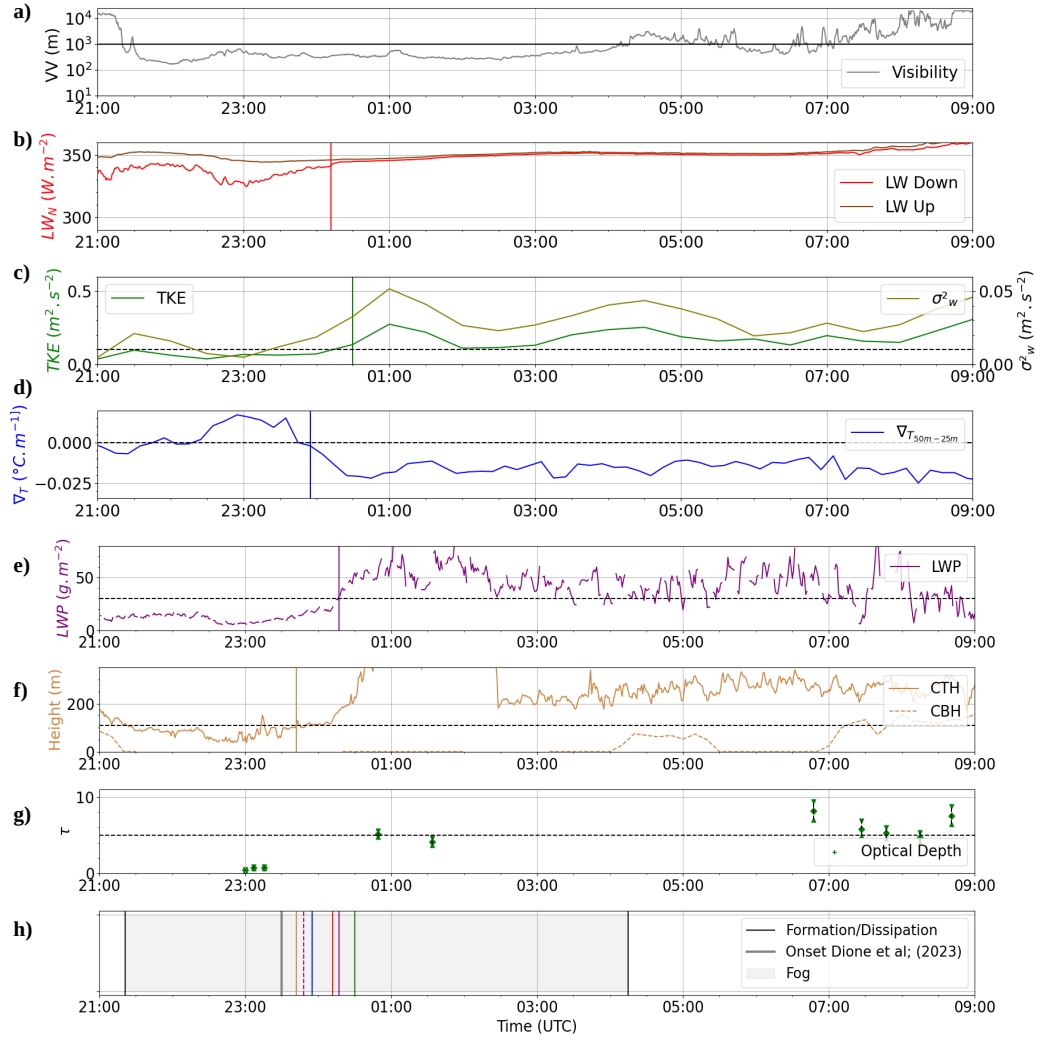
Figure 2. Time series for IOP 14 fog event : (a) visibility (b) downward (light red) and upward (brown red) longwave radiative fluxes, (c) TKE (green) and σ_w^2 (light green), (d) vertical gradient of temperature between 25 and 50 m from the MWR, (e) LWP from the MWR, (f) CTH from the BASTA cloud radar and CBH from the ceilometer, and (g) optical depth from the CDP. In panels (c) to (g), threshold values are indicated by the dotted horizontal lines. In panels (b) to (f), the vertical segments represent the transition ending times. (h) Summary graph with the five transition ending times and their respective colours superimposed over the foggy period (grey area) delimited by the formation and dissipation times in vertical black lines. Onset of the transition phase following Dione et al. (2023) is indicated by a thick vertical grey line. The vertical purple dotted segment represents the transition ending time derived from the LWP with a threshold of 15 g.m^{-2} instead of 30 g.m^{-2}.

ending is systematically associated with an increase in LW_N, TKE, LWP, CTH and a decrease in the vertical temperature gradient. For this case, the different transition time ending values are very close within a 48-min period around midnight,

leading to a short transition phase duration ranging between 12 minutes (CTH, orange) and 1 hour (TKE, green). But there could be large discrepancies. Figure A1 presents the results for IOP 11 where Dione et al. (2023) determined the onset of the transition phase at 2300 UTC, while ending times are distributed from 0030 UTC to 0055 UTC, except the 30 $g.m^{-2}$ LWP threshold about two hours later. This threshold seems too high in this case since the transition rather ends when LWP reaches 15 $g.m^{-2}$. The transition phase duration is longer for this case, from 1h30 to 1h55, but it is not associated with a higher uncertainty on the ending time, which is shorter than for IOP 14 (Tab. 2). Furthermore, we do not observe a significant increase in optical thickness during the transition phase, with values not exceeding 2 until the fog dissipates at 0349 UTC. Indeed, we will see in Sec. 5 that these low values of optical depth while the fog is optically thick result from the sedimentation process. IOP 6 reveals the largest uncertainty on the transition phase ending (Fig. A2) with the LW flux exceeding 5 $W.m^{-2}$ very early (50 min) after the fog onset, about 2h30 before the TKE threshold, and 3h30 before both CTH and vertical temperature gradient thresholds. This appears to be mainly due to advective processes that perturbed the fog life cycle. Indeed all these parameters are also close to their respective thresholds (CTH = 87.5 m, TKE = 0.06 $m^2.s^{-2}$ and vertical temperature gradient = 0.0007 $°C.m^{-1}$) but the vertical development of the fog layer is temporarily stopped as the surface wind decreased before its direction shifted from SW to SE (Fig. 11a). The fog started to deepen again around midnight and then all parameters reached their thresholds shortly after, except the 30 $g.m^{-2}$ LWP threshold which required 1h15 more. The optical depth follows a similar evolution with values close to 2 shortly after fog formation, decreasing to 0.32 and 0.21 for profiles # 4 and # 5, respectively, around 2300 UTC when the vertical development is stopped, and increasing again after midnight during the second vertical development, with values up to 6. The threshold of 5 seems then too high since values are closer to 2 when fog is optically thick shortly after fog formation. Dione et al. (2023) defined the onset of the transition phase at 0000 UTC, which actually corresponds to the second period of thick fog. Consequently, for this case, the onset remained undefined. This illustrates the difficulty to define accurate thresholds for complex fog life cycles. Finally, during IOP 9a (not shown), which was not examined by Dione et al. (2023), LW_N indicates that the fog is already thick at its formation, due to the immediate condensation of liquid water over a 80 m thick layer, but with a rather low value of LWP < 5 $g.m^{-2}$. A cloud passing above temporarily caused the fog layer to drop below 50 m, and as for IOP 6, other parameters then exceed their thresholds later on when the fog started to deepen again, resulting in a transition ending time uncertainty of 2h29 as indicated in Table 2.

For these four cases, transition phase ending occurred with LWP values systematically much lower than the 30 $g.m^{-2}$ threshold. To be consistent with the other parameters, we find that a value of 15 $g.m^{-2}$ is more suited to detect the transition ending. The other estimations are in agreement during IOPs 11 and 14 during which there was a clear thin-to-thick transition phase ending period shorter than 1h, but they are more dispersed during IOPs 9a and 6c while the fog became optically thick immediately after its formation or shortly after, respectively. As a result, no tendency is observed between the time interval during which the different thresholds are reached and the duration of the transition period. This suggests that multiple thresholds reached in a short period of time do not seem to favour a rapid thin-to-thick transition and, conversely, that a slow transition is not systematically associated with inconsistencies between all the thresholds. In addition, these four cases do not reveal any trend in the order of exceeding the thresholds by the different parameters. Furthermore it appears that non-local processes such as the change in wind orientation or the advection of clouds can disrupt the usual fog life cycle by stopping the vertical

development of the fog layer. Finally, evolution of the optical depth revealed a strong increase at the transition during IOP 14,
270 while lower values are found for IOPs 11 and 6. The threshold of 5 appears then too high, and we find that a value of 2 is more
appropriate to discriminate between optically thin and thick fogs. Note that this value is consistent with retrievals reported by
Guy et al. (2023) from spectral measurements of downwelling longwave radiation performed with the Atmospheric Emitted
Radiance Interferometer (AERI). For the 12 optically thin fogs sampled in central Greenland, including 9 mixed-phase cases,
most of the 5-min liquid and ice optical depth retrievals are much lower than 2, with median values of 0.8 and 0.5, respectively.
275 This analysis provides estimations of the transition phase duration for each case with an associated period of uncertainty,
independent of the in situ measurements performed under the tethered balloon. These are now examined to document the evo-
lution of the vertical profile of microphysical properties during the fog life cycle, with particular emphasis on fog adiabaticity.

3 Fog adiabaticity

3.1 Equivalent adiabaticity from closure and parameterization as a function of CTH

280 In adiabatic liquid clouds, the liquid water content increases almost linearly with the altitude as $LWC(z) = \Gamma_{ad}(T,P)(z-Zb)$,
where $\Gamma_{ad}(T,P)$ is the condensation rate that depends on pressure P and temperature T at the cloud base (Betts, 1982; Albrecht
et al., 1990; Brenguier, 1991) following:

$$\Gamma_{ad}(T,P) = \rho_d \left(\frac{(\epsilon + w_s) w_s l_v \Gamma_w}{R_d T^2} - \frac{g w_s P}{(P - e_s) R_d T} \right) \tag{2}$$

with l_v the latent heat of vaporization, g the acceleration of gravity, R_d the dry air ideal gas constant, ϵ the ratio between the
285 dry air to water vapor ideal gas constant equal to 0.622, e_s the vapor saturation pressure, w_s the saturation mixing ratio, ρ_d the
dry air density, and Γ_w is the moist adiabatic lapse rate given in Eq. 3 (Hummel and Kuhn, 1981):

$$\Gamma_w = \frac{g}{c_p} \frac{1 + \frac{l_v w_s}{R_d T}}{1 + \frac{\epsilon l_v^2 w_s}{R_d c_p T^2}} \tag{3}$$

with c_p the specific heat of dry air at constant pressure.

The liquid water path of a cloud layer is the total amount of liquid water, as :

$$LWP = \int_{Zb}^{Zt} LWC(z) dz \tag{4}$$

In shallow convective cloud where the condensation rate can be assumed relatively constant, it follows (Albrecht et al., 1990)
: $LWP_{ad} = \frac{1}{2} \Gamma_{ad}(T,P)(Zt - Zb)^2$.

Processes such as entrainment-mixing of dry air or precipitation formation, however, tend to reduce LWC values, and Betts
(1982) introduced the in-cloud mixing parameter β to reduce the condensation rate as $(1 - \beta)\Gamma_{ad}(T,P)$. Many studies have

quantified departure from the adiabatic values using aircraft in situ data and revealed that the reduction in stratiform clouds is much lower than in cumulus ones and results mainly from mixing at the cloud top and drizzle formation (Gerber, 1996; Wood, 2005; Brenguier et al., 2011; Braun et al., 2018). By using remote sensing instruments in shallow stratocumulus clouds, Albrecht et al. (1990) also noticed a large reduction in LWP, compared to the adiabatic values, when drizzle is observed. Observations in fog are rare due to the difficulty of measurement, but previous studies have reported LWC profiles that are fairly constant or increase with height in a well-developed fog layer (Okita, 1962; Pinnick et al., 1978; Price et al., 2015; Egli et al., 2015).

To retrieve the cloud base from satellite data, allowing discrimination between low stratus and fog, Cermak and Bendix (2011) developed a subadiabatic model of cloud microphysics. They derived a complex cloud profile parameterization used for LWP computation by dividing the cloud in three layers with different β values to account for processes reducing the LWC near the ground, in the central region and at cloud top.

Recently, to improve nowcasting of fog dissipation, Toledo et al. (2021) developed a one-column conceptual model of adiabatic continental fog by assuming that the LWC linearly increases with height with a reduced condensation rate expressed as $\alpha(z)\Gamma_{ad}(T,P)$ where $\alpha(z)$ is the local adiabaticity. The LWP of a fog layer is then computed considering that the equivalent adiabaticity $\alpha_{eq} = 1 - \beta$ remains constant throughout the fog layer from the ground to the CTH, as:

$$LWP = \frac{1}{2}\alpha_{eq}\Gamma_{ad}(T,P).CTH^2 + LWC_0.CTH \tag{5}$$

where LWC_0 is the LWC value at the ground.

Toledo et al. (2021) then used data from 7 years of measurements performed at the SIRTA (Site Instrumental de Recherche par Télédétection Atmosphérique) observatory near Paris, to compute this equivalent adiabaticity α_{eq}. Without measurements of the vertical profiles of LWC, they used an inversion of Eq. 5 to calculate α_{eq} by closure as :

$$\alpha_{eq}^{closure} = \frac{2(LWP - LWC_0.CTH)}{\Gamma_{ad}(T,P).CTH^2} \tag{6}$$

where LWP and CHT are provided by a HATPRO MWR and a BASTA radar, respectively, and LWC_0 is derived from the measured visibility at ground by the parameterization developed in Gultepe et al. (2006).

$\alpha_{eq}^{closure}$ is then the equivalent adiabaticity that would give the same LWP in the fog layer, but assuming a linear increase in LWC with height. Note that from Eq. 6, $\alpha_{eq}^{closure} = 0$ corresponds to a constant LWC profile equal to LWC_0 from the ground to CTH and is quite different from $\beta = 1$, which corresponds to the total evaporation of the cloud due to mixing with clear air (Betts, 1982). Toledo et al. (2021) found that $\alpha_{eq}^{closure}$ depends mainly on the CTH, converging to ≈ 0.7 for developed fogs, and pointed out that thinner fog with LWP values lower than 20 g.m^{-2} has $\alpha_{eq}^{closure}$ values below 0.6 and can even reach negative values. They thus proposed the following parameterization :

$$\alpha_{eq}(CTH) = \alpha_0(1 - e^{-\frac{CTH-H_0}{L}}) \tag{7}$$

where $\alpha_0 = 0.65$, $H_0 = 104.3$ m and L = 48.3 m.

Dione et al. (2023) used this parameterization to analyze the four deepest fogs of SOFOG3D. They revealed negative values of $\alpha_{eq}(CTH)$ during the stable phase, which increase from 0 to 0.5 during the thin-to-thick transition and finally exceeds 0.5 when LWP > 20 g.m^{-2}. Therefore, analysis of $\alpha_{eq}(CTH)$ enables to discriminate between optically thin and thick fog, characterized by negative and positive values respectively.

330   Note that negative adiabaticity values result mathematically from high LWC_0 values at the surface and low LWP of the fog layer. This reflects that the LWC profile is not increasing with height, and consequently that the basic assumption of the conceptual model is not valid. We now use the CDP measurements to analyze fog adiabaticity derived from in situ measurements.

3.2   Vertical profiles of LWC and temperature from in situ measurement

Droplet size distribution recorded by the CDP under the tethered balloon during SOFOG3D allows us to retrieve vertical
335   profiles of LWC in the fog layer and then to examine the actual fog adiabaticity and compare to the equivalent values derived by closure.

Figure 3 presents vertical profiles of LWC and temperature measurements collected during IOP 14 (upper panels) and IOP 11 (lower panels). Boxplots correspond to statistics computed within 5 m height layers from the ground up to the fog top. Black lines indicate the adiabatic theoretical calculation of LWC and lapse rate, from Eq. 2 and 3 respectively.

340   The ascent of IOP 14 was performed between 0611 and 0647 UTC, about 6 hours after the fog became optically thick (Fig. 2) and 2 hours before its dissipation in stratus (profile # 6 of Fig. 9d). As a general trend, LWC values increase with the altitude up to 215 m, before they drop suddenly in the upper fog layers near the fog top at 255 m (Fig. 3a). In this deep fog, however, we can observe that the increase of LWC is not continuously monotonic, with the presence of a layer with much lower LWC values at heights between 120 and 170 m. The vertical profile of temperature decreases almost regularly with height up to the
345   fog top (Fig. 3b). Unfortunately, the balloon failed to cross the summit due to the increase in wind speed to over 6 m.s^{-1}, but the radiosonde launched 35 minutes earlier indicates a sharp temperature inversion of -1.5 °C (not shown). These observations are consistent with previous measurements in well-mixed fog layer revealing mainly adiabatic vertical profiles of LWC and temperature, but also a sharp reduction in LWC at the fog top probably due to entrainment-mixing of dryer air in the upper fog layers.

350   In contrast, the descent during IOP 11 between 2209 and 2223 UTC reveals a reverse trend with LWC being maximal at the ground, around 0.11 g.m^{-3}, and decreasing with altitude up to the CTH at 55 m, except a thin slice around 40 m. It is associated with a stable vertical profile of temperature that increases from 8.5 °C at ground to 10.1 °C above the CTH. Indeed at this time (profile # 2 of Fig. 10d) the fog is still optically thin as the transition to thick fog will occur about 1 hour and a half later. Such reverse LWC profiles were almost systematically observed in optically thin fogs during the SOFOG3D campaign
355   and are investigated in more details in section 4. These results highlight contrasting vertical profiles between well-mixed fogs, whose characteristics can be correctly represented by the adiabatic model, and thin fogs exhibiting an opposite trend.

For LWC profiles, the linear increase corresponding to $\alpha_{eq}^{closure}$ calculated from Eq. 6 following Toledo et al. (2021) is plotted in dashed blue line with values of 0.48 and 1.02 for IOP14 and IOP11, respectively. It is worth noting that these values differ from the values of $\alpha_{eq}(CTH)$ derived from the parameterization as function of CTH (Eq. 7) used by Dione et al. (2023).
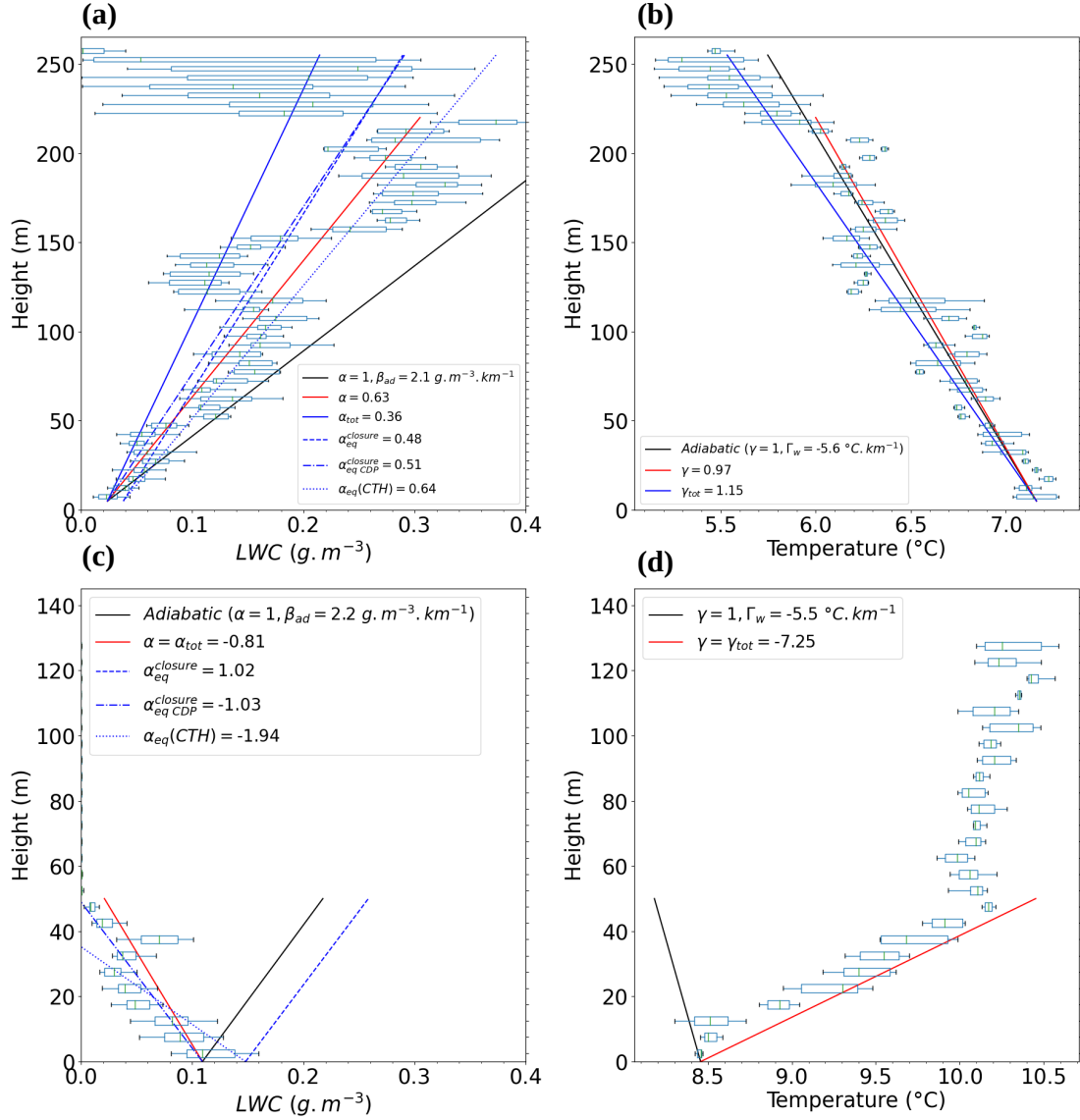
Figure 3. Vertical profiles of (left) LWC and (right) temperature measured during (a and b) a descent of IOP 14 between 0611 UTC and 0647 UTC and (c and d) a descent of IOP 11 between 2209 UTC and 2223 UTC. Boxplots are derived from data collected within 5 m height layer. Adiabatic values are indicated by a black line. Adiabaticity calculated over the entire profile and over the profile truncated at the altitude of the maximum of LWC are indicated by a solid blue and a red line, respectively. The equivalent adiabaticity from closure (Eq. 6) retrieved by remote sensing ($\alpha_{eq}^{closure}$) and in situ measurements ($\alpha_{eqCDP}^{closure}$) are indicated by a dashed and dash-dotted blue line, respectively, while the equivalent adiabaticity derived from the parameterization as a function of CTH (Eq. 7) is indicated by a dotted blue line.

As expected for the well-mixed fog case, the resulting profile of LWC tends to underestimate actual values of LWC in the lower part of the layer with predicted values that can be half the measured ones. The dotted and long dashed blue line corresponds to the fog adiabaticity from closure but computed with the CDP data $\alpha_{eqCDP}^{closure}$ (see next section), and produces a very similar result. Indeed, these low values of $\alpha_{eq}^{closure}$ result mainly from the strong reduction of LWC at the fog top. Consequently, the corresponding profiles of $\alpha_{eq}^{closure}$ are not really representative of the global agreement of the measured LWC with the adiabatic model. An overall agreement is, however, clearly reflected on the temperature (Fig. 3b), the adiabaticity (blue) being less affected by the evaporation following the mixing below the fog top. The profile of $\alpha_{eq}(CTH)$, represented by a dotted blue line, enables to retrieve an equivalent adiabaticity more in agreement with the general trend of LWC with altitude. The value of 0.64 is close to the asymptote of the parameterization ($\alpha_0 = 0.65$) due to a high CTH reaching 255 m. Surprisingly, the reverse LWC profile of IOP 11 is well reproduced with data aligned along the negative slope -1.03 of $\alpha_{eqCDP}^{closure}$. In contrast for this case, $\alpha_{eq}^{closure}$ is positive due to a larger LWP value provided by the MWR (7.12 g.m^{-2}) compared the CDP measurements (2.67 g.m^{-2}) and the profile is shifted to larger LWC due to an larger value of LWC_0 provided by the parameterization of Gultepe et al. (2006) (0.15 g.m^{-3}) compared to the CDP measurements (0.11 g.m^{-3}). In addition, $\alpha_{eq}(CTH)$ reveals a negative value of -1.94 in agreement with $\alpha_{eqCDP}^{closure}$ and the general trend of LWC with height, related to a low CTH value of 55 m. These observations indicate that for optically thin fogs characterized by low LWP values (LWP < 10 g.m^{-2}), uncertainties on LWP measurements and LWC_0 retrievals induce inconsistencies between LWP, CTH and LWC_0 values, which implies that the closure conditions required for the calculation of $\alpha_{eq}^{closure}$ are not satisfied.

To better estimate the agreement of the measurements with the adiabatic model, we calculate the adiabaticity parameters α and γ with respect to LWC and lapse rate, respectively, by determining the slope of the linear regression between medians values of the statistics at each altitude range and dividing by Γ_{ad} and Γ_w, respectively. To avoid underestimation of adiabaticity resulting from entrainment-mixing processes below the fog top for well-mixed fog, we discard this layer by truncating the vertical profile at the altitude where LWC reaches its maximum value. The corresponding profiles are superimposed as red lines on Fig. 3a and b. With such a procedure α = 0.63 for IOP 14, close to $\alpha_{eq}(CTH)$, and the corresponding fit to the measurements better represents the general shape of the vertical profile than $\alpha_{eq}^{closure}$ and $\alpha_{eqCDP}^{closure}$. In addition, taking into account the entrainment-mixing layer above 220 m reduces strongly the adiabaticity to $\alpha_{tot} = 0.36$ (solid blue line). Thus, the adiabaticity derived by truncating the entrainment-mixing layer for well-mixed buoyant fogs seems to be a relevant metric to characterize the global deviation of the LWC profile from the adiabatic one. For the lapse rate $\gamma = 0.97$ which is then very close to the adiabatic decrease. In contrast, the descent during IOP 11 reveals negative α and γ values of -0.81 and -7.25 respectively.

In a first step, we take advantage of the 140 selected profiles to evaluate the agreement between $\alpha_{eq}^{closure}$, $\alpha_{eq}(CTH)$ and the equivalent values derived from in situ data.

3.3 Comparison between equivalent fog adiabaticity estimations

For each vertical profile, $\alpha_{eq}^{closure}$ is computed from Eq. 6 by using the median values over the duration of the profile of CTH from the radar, LWP from the MWR and visibility meaurements. Due to an instrument failure, data from the visibilimeter deployed at the Charbonnière site were only available for IOPs 9a to 13b. As for the other 7 IOPs, the visibilimeter at the Jachère

site (at 1.4 km) must be used. To compute the fog adiabaticity from closure with CDP data, $\alpha_{eqCDP}^{closure}$, CTH is determined by using an LWC threshold of 0.01 g.m^{-3}, the LWP is calculated by integrating the median value of LWC in each altitude range up to CTH, and LWC_0 is defined as the median value of LWC in the lowest altitude range. The median height corresponding to LWC_0 is 3.5 m with 1st and 3rd quartiles of 2.5 m and 6.2 m, respectively, i.e. very close to the height of the visibilimeters deployed at 3 m above ground level, but over a short time period typically of about ten seconds. Except for CTH_{CDP}, the 1st and 3rd quartiles of the distribution of each parameter are calculated for each vertical profile, to assess the variability during the corresponding time interval.

Comparison of $\alpha_{eqCDP}^{closure}$ vs. $\alpha_{eq}^{closure}$ are reported on Fig. 4a and reveal large discrepancies, with very low values of the coefficient of determination R^2 and the slope of the linear regression which reach 0.18 and 0.35, respectively. The first available gate of the radar being 37.5 m, it obviously can not detect CTH below this height. In total 21 profiles performed by the tethered balloon are lower than this limit, that is about 20 % of the data set. This provides an additional motivation to compute $\alpha_{eqCDP}^{closure}$ in order to evaluate the conceptual approach against the actual vertical profile for the thin layers which correspond to the formation phases of many radiation fog events in stable conditions. For LWP retrieved from the MWR measurements, caution should be taken when clouds above the fog layer were detected, because it is not possible to dissociate the LWP values of the fog layer and of the cloud layer above. Therefore, due to the presence of clouds above fog during IOP 2b and IOP 6a, these two cases were discarded. Finally, profiles within stratus cloud have been also removed to allow calculation of $\alpha_{eq}^{closure}$. In total the dataset is then reduced to 79 profiles. Note that both methods lead to values of $\alpha_{eq}^{closure} > 1$ but not for the same cases. This suggests that such values result from inaccuracy in measurements rather than reflecting superadiabatic conditions.

Sensitivity tests are carried out on LWP, CTH and LWC_0, by modifying only one of the 3 variables in Eq. 6 using the CDP measurements, the other two remaining based on $\alpha_{eq}^{closure}$ calculation in order to determine which parameters introduce the most dispersion in the comparison. Discrepancies seem less related to CTH as the sensitivity test on this variable presents a satisfactory correlation with an R^2 value of 0.68 (Fig. 4c). For this parameter, for which no variability from the CDP measurements can be calculated, the worst cases, from IOP 9b and 13b are mainly due to overestimation of CTH by the radar for actual CTH just above its detection limit that results in overestimation of $\alpha_{eq}^{closure}$. Then, sensitivity test on LWP shows a lower but correct correlation with an R^2 value of 0.58 (Fig. 4b). Indeed comparison of LWP provided by the MWR compared to the CDP measurements reveals a very good agreement for values below 15 g.m^{-2}, but some differences are observed for well-mixed fogs characterized by the highest LWP values (not shown). The worst cases on Fig. 4b (2 green points) corresponds to the IOP 11 profiles with LWP from CDP much lower than the MWR value and highlights the impact of such difference. Note that the variability represented by 1st and 3rd quartiles is relatively small compared to the dispersion and similar for both estimates, indicating that the temporal variability of LWP during the profile does not have a significant impact on the derived value of adiabaticity by closure. Finally, large differences are observed when LWC_0 is replaced by the CDP values : Fig. 4d shows that there is a strong increase of the scatter of the data, consistent with a poor value of the coefficient of determination of 0.51. Indeed, the comparison of LWC_0 values is reported in Fig. 5 which reveals large discrepancies with a coefficient of determination as low as 0.42. The slope of the regression is 0.63 (Fig. 5) but this likely results from the large scatter of the data and it is not clear that the parameterization of Gultepe et al. (2006) with visibility measurements tends to produce systematically
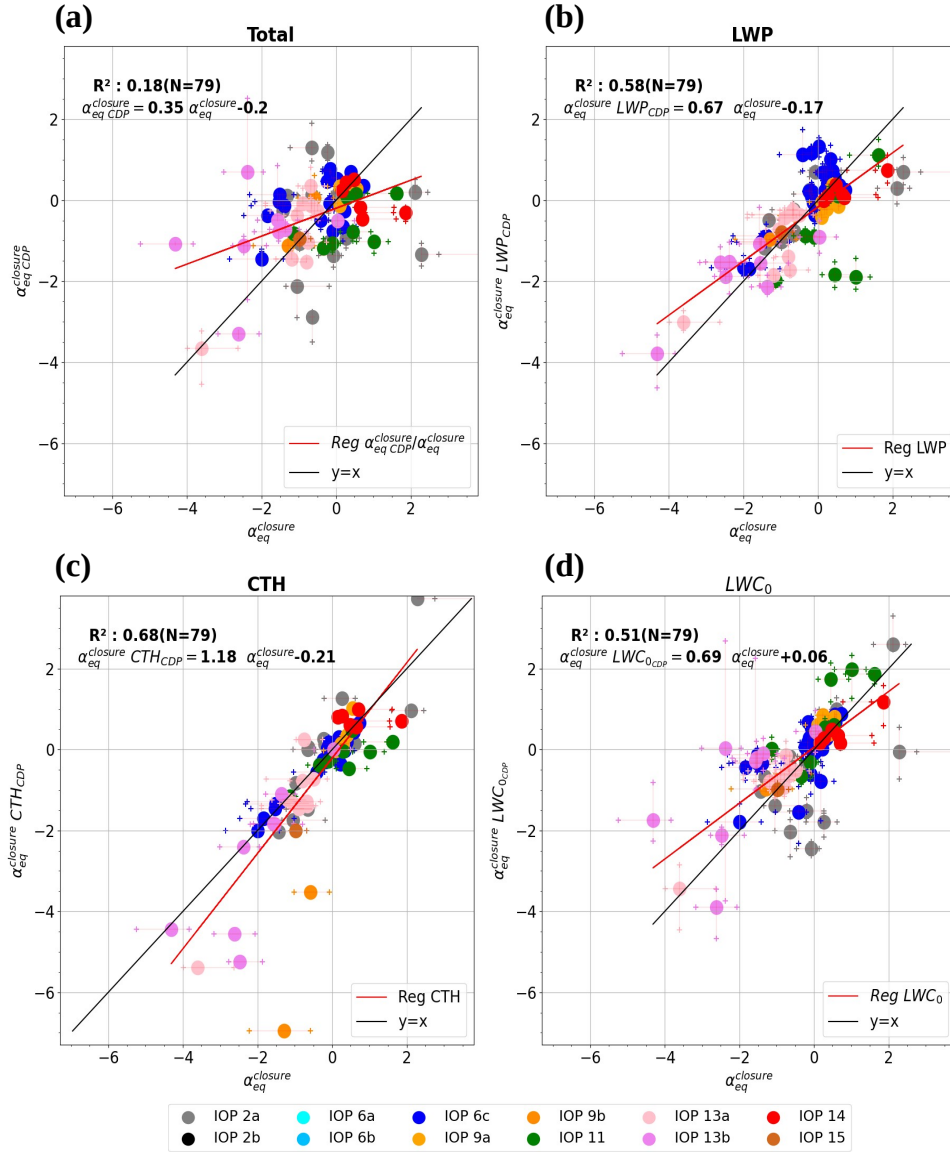
Figure 4. Fog adiabaticity from closure values comparison : (a) $\alpha_{eq}^{closure}$ values derived from the CDP measurements as a function of $\alpha_{eq}^{closure}$. Sensitivity tests performed on $\alpha_{eq}^{closure}$ when using only one parameter derived from CDP measurements: (b) LWP, (c) CTH, and (d) LWC_0. Colour of dot and crosses representing 1st and 3rd quartiles, depends on IOP as indicated in the legend.

LWC values larger than the CDP measurements. Part of the discrepancies could arise from temporal fluctuations of LWC_0
430 during the time taken by the balloon to complete each profile, which cannot be truly inferred from the CDP measurements. It is also likely that the use of the visibility measurement from the Jachère site for 7 out of the 12 IOPs studied contributes to the dispersion. Therefore, these sensitivity tests reveal that the discrepancies between $\alpha_{eq}^{closure}$ and $\alpha_{eqCDP}^{closure}$ arise both from the
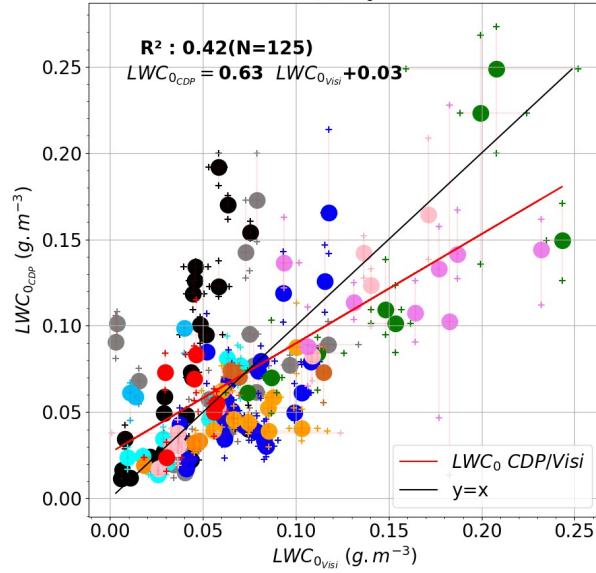
Figure 5. LWC_0 derived from the CDP measurements as a function of LWC_0 derived from the visibility measurements at the Jachère site using the parameterisation defined in Gultepe et al. (2006). Colours of dot and crosses representing 1st and 3rd quartiles, corresponding to IOP are given in Fig. 4.

LWC_0 values derived from visibility measurement and by differences in LWP between the CDP and the MWR. Note also that the data on Fig. 4a are not completely distributed in the same way as in Fig. 4b,d, reflecting that some differences between the parameters compensate for each other.

Toledo et al. (2021) have shown the dependency of $\alpha_{eq}^{closure}$ on LWP and CTH, for which a parameterization as a function of CTH was proposed (Eq. 7). We therefore examined evolution of $\alpha_{eqCDP}^{closure}$ as a function of LWP and CTH issued from the CDP measurements for our dataset in Fig. 6 where measurements in stratus clouds have been excluded for consistency with previous studies. The observations reveal similar trend with mainly negative values of $\alpha_{eqCDP}^{closure}$ when LWP < 5 g.m^{-2}, which represent 67 % of the sampled profiles. Note that some values reach -4, much lower than those reported in Toledo et al. (2021). Indeed they correspond to very thin layers with CTH in the blind zone of the radar BASTA. Except for two profiles of IOP 11 (green dots), $\alpha_{eqCDP}^{closure}$ is always positive when LWP exceeds 10 g.m^{-2}. Surprisingly, these two profiles of IOP 11 correspond to large values of CTH (Fig. 6b). Indeed we will see in section 5 that these particular reverse profiles of LWC result from the sedimentation process. Beyond a LWP of 15 g.m^{-2}, $\alpha_{eq}^{closure}$ tends to converge around 0.5, but the number of samples is too limited for a precise evaluation of this limit. Two cases from IOP 2a exhibit superadiabatic conditions with $\alpha_{eqCDP}^{closure} > 1$. In fact, these profiles correspond to a particular case where the condensation of liquid water at the fog formation occurred first at altitude before the surface which therefore distorts the slope calculation (see Fig. C1).

The evolution of $\alpha_{eqCDP}^{closure}$ as a function of CTH depicted in Fig. 6b is very similar. The parameterization of Toledo et al. (2021) has been defined for CTH > 85 m corresponding to the first gate of the radar used at the SIRTA site. This limit has
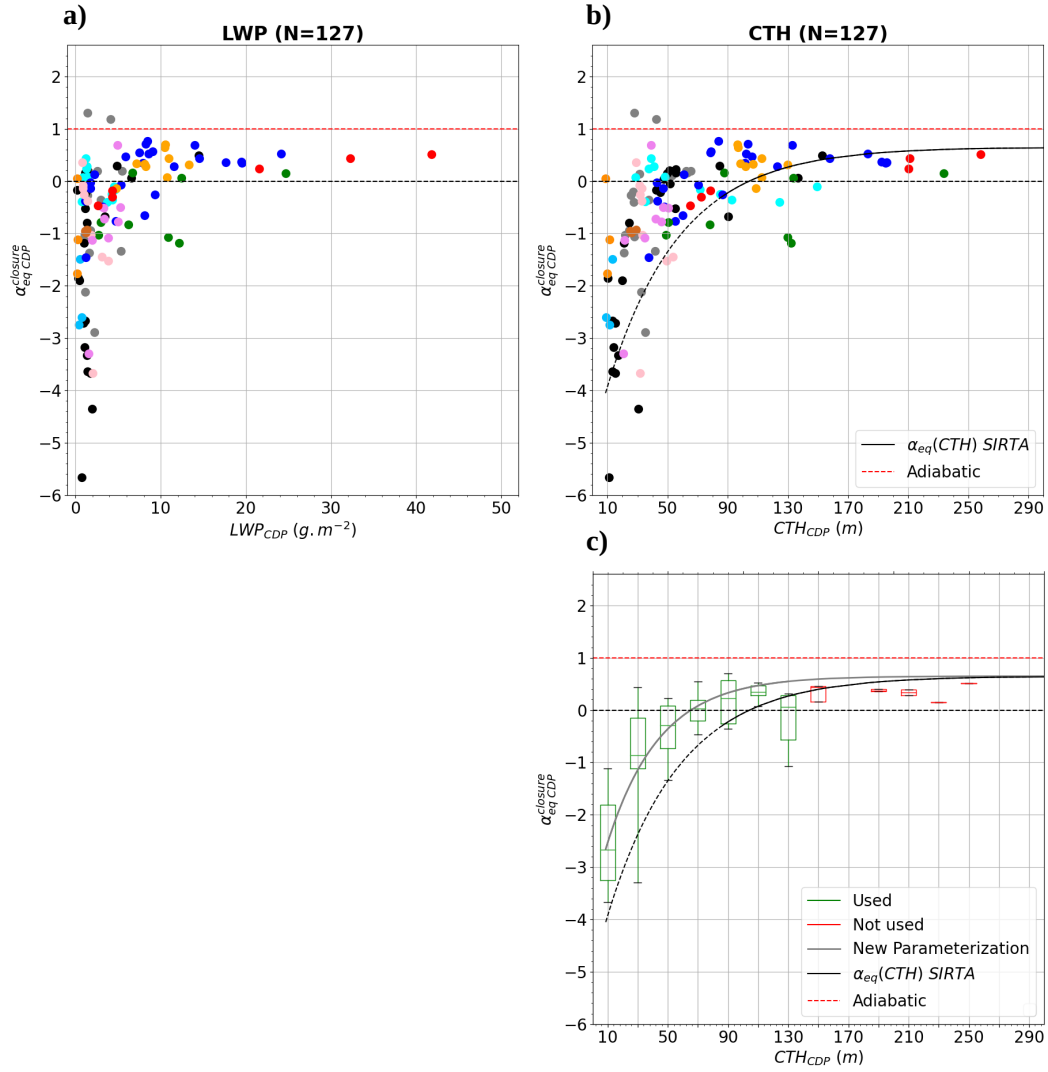
Figure 6. Equivalent adiabaticity from closure derived from CDP as a function of (a) LWP and (b) CTH. Each IOP is indicated with a specific colour as indicated in the legend of Fig. 4. (c) Boxplot of $\alpha_{eq\,CDP}^{closure}$ for each CTH range of 20 m. The parameterization of Toledo et al. (2021) and new one based on the SOFOG3D observations are superimposed by a black and grey curve respectively. The samples used (respectively not used) in the new parameterization are indicated by green (red) boxplots. The extension of the parameterization of Toledo et al. (2021) outside its range of validity is represented by a dashed line. The red line marks the adiabatic value.

450   been extended here to 10 m (dashed line) to compare with in situ data : most of them are located above this curve reflecting that positive values of $\alpha_{eqCDP}^{closure}$ can be observed for CTH lower than 85 m. Statistics on classes of 20 m width indicate that the median of $\alpha_{eqCDP}^{closure}$ values is positive when CTH > 70 m (Fig. 6c). For CTH > 150 m, $\alpha_{eqCDP}^{closure}$ values fluctuate around 0.4. This limit is lower than the convergence values of 0.65 and 0.6 reported for fog conditions in Toledo et al. (2021) and

Dione et al. (2023), respectively. However, the number of profiles sampled in such developed fogs is obviously too limited here to derive significant convergence. Note that calculations of $\alpha_{eq}^{closure}$ with remote sensing measurements for the same profiles exhibit the same trend and do not improve the convergence estimation (Fig. B1). This attests that lower values of $\alpha_{eq}^{closure}$ for well-mixed deep fogs in our dataset do not result from the type of instrument used to compute adiabaticity from closure (in situ or remote sensing) but reflect the actual properties of the fogs sampled during SOFOG3D. Following Toledo et al. (2021) a parameterization of α_{eq} as a function of CTH is derived by minimizing Eq. 7 with respect to the median value of α_{eq} for each CTH range of 20 m. Only intervals with more than 5 valid samples are used. Given the lack of valid samples for CTH > 140 m (Fig. 6c, green boxplots), the α_0 asymptotic value is set to 0.65 as determined by Toledo et al. (2021). Thus, only the parameters H_0 and L from Eq. 7 are determined, which represent the typical CTH values at which LWC increases with height ($\alpha_{eq} = 0$) and at which the thin-to-thick transition begins ($\alpha_{eq} = 0.5$), respectively. The retrieved values, $H_0 = 65.3$ m and L= 34.8 m, are lower than the values obtained by Toledo et al. (2021), 104.3 and 48.3 m, respectively. Therefore, the thinner fog layers sampled during SOFOG3D suggest that fog become optically thick at lower CTH than previously derived from SIRTA observations.

In summary, the comparison of equivalent fog adiabaticity from closure calculations reveals that, despite the large variability that results mainly from LWC_0 and LWP retrievals, the distribution of equivalent fog adiabaticity is approximately the same between in situ or remote sensing measurements and the Toledo et al. (2021) approach. Additionally, in situ data allow to characterize large negative $\alpha_{eq}^{closure}$ values relative to thin fogs, for which a new parameterization as a function of CTH has been proposed. We now focus on in situ CDP data to examine relationships of equivalent fog adiabaticity with the actual adiabaticity.

3.4 Comparison between α, $\alpha_{eq}^{closure}$ and $\alpha_{eq}(CTH)$

We introduced at section 3.2 a calculation of the adiabaticity α by fitting CDP measurements (red lines in Fig. 3a,c). The diluted layer just below the top is not taken into account to represent the general shape of the LWC vertical profiles. The main objective is now to derive a synthetic parameter to better quantify departure from the adiabatic model and document its evolution during the fog life cycle. To perform a quantitative evaluation of this parameter, we extend the analysis to the 140 selected profiles of the campaign. The thermodynamical and microphysical properties of each vertical profile are calculated with a vertical resolution of 5 m for episodes that experienced thin-to-thick transition. For fogs that remained thin and very thin (less than 10 m) throughout their life cycle, the vertical resolution is increased to 3 m and 1 m, respectively. Except for very thin fog episodes, the minimum number of 1 Hz CDP samples required to calculate the statistics over each altitude range was set to 5. Given that, the average speed of the tethered balloon is about 0.5 m.s^{-1}, this represents a height of about 3 m corresponding to the vertical resolution required for most vertical profiles. Then, α and γ are calculated only on representative vertical profiles gathering at least 5 different altitude ranges. As discussed above, the diluted region below CTH is removed for the well-mixed fog. For doing so, α is first calculated over the entire profile. Cases with $\alpha > 0.1$ are identified as increasing with height and α is therefore recalculated on the lower part of the profile delimited by the maximum median LWC values, otherwise there are classified as reverse profile.
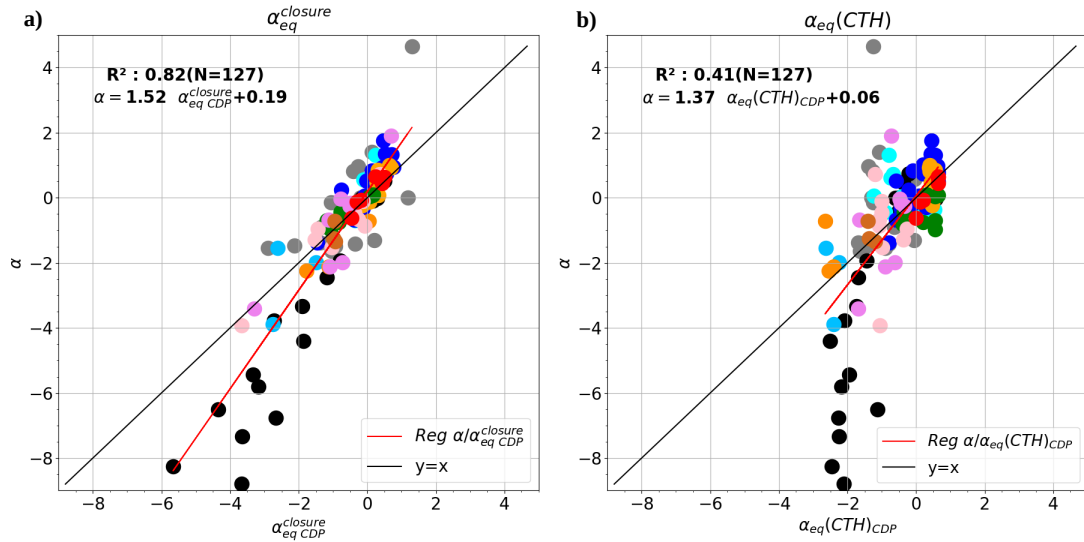
Figure 7. Adiabaticity α as a function of the equivalent adiabaticity (a) from closure issued from the CDP measurements (b) based on the parameterization as a function of the CTH from the CDP using the values retrieved in the previous section for H_0 and L. Each IOP is indicated with a specific colour from IOP 2a to IOP 15 given in Fig. 4.

Comparison of α with $\alpha_{eqCDP}^{closure}$ (Eq. 6) and $\alpha_{eq}(CTH)_{CDP}$ from the new parameterization are reported on Fig. 7 for the 127 selected profiles in fog. As expected, the absolute values of α are generally larger than those of $\alpha_{eqCDP}^{closure}$ and $\alpha_{eq}(CTH)_{CDP}$,

490 as attested by the slope of linear regression of 1.52 (Fig. 7a) and 1.37 (Fig. 7b), respectively. Removing the diluted region at fog top for well-mixed fog increases α values. However only a few samples over the 32 profiles identified as increasing with height are significantly impacted and the comparison with α calculated over the entire profile leads to very similar results (not shown). Some values of α exceed 1 but the examination of such profiles does not reveal any superadiabatic growth. In fact, these values rather result from the uncertainties of the method, which could be very sensitive to the highest values of LWC

495 below the top or LWC_0 at the bottom (see profiles # 6 and # 7 of IOP 6 on Fig. 11 for example). This is particularly the case for the first profile of IOP2a (in grey), where high values of LWC > 0.1 g.m^{-3} at 20 m height while condensation at the surface has not yet taken place, lead to an α as high as 4.66 as depicted in Fig. C1c. In contrast, given that CTH only reaches 30 m, the parameterization leads to a negative value of $\alpha_{eq}(CTH)_{CDP}$ (Fig. 7b). Indeed, as a general trend, the parameterization generates too much negative adiabaticity values due to low values of CTH, while $\alpha_{eqCDP}^{closure}$ are positive in agreement with

500 α. In contrast for thinnest layers, $\alpha_{eq}(CTH)_{CDP}$ remained larger than -3 that are clearly overestimated compared to α and $\alpha_{eqCDP}^{closure}$. Fitting the CDP data produces higher negative values for such reverse LWC profiles. Appendix C1a illustrates the corresponding profile for one of the lowest values (α = -8.3) obtained during IOP 2b, which appears to be realistic given the linear regression on the vertical profile of LWC. Note that for such thin fog layer of 10 m height, the LWP is only 0.7 g.m^{-2} although LWC_0 reaches 0.1 g.m^{-3}. Therefore $\alpha_{eq}^{closure}$ appears to be a better predictor of fog adiabaticity, with an R^2 value

of 0.82, since the parameterization taking only CTH into account does not allow to retrieve positive adiabaticity values of optically thin fogs, and overestimates minimum values of thinnest fogs, leading to an R^2 value of 0.41.

Reverse LWC profiles for thin fogs were frequently observed during the experiment and are mainly associated with stable atmospheric conditions resulting from radiative cooling established before the fog formation phase. As a next step, the evolution of vertical profiles during the fog life cycle is now studied in more detail to determine to what extent LWC profiles correlate with temperature profiles and how they both evolve during the thin-to-thick transition, when it exists, towards the adiabatic shapes of well-mixed fog layers.

4 Evolution of vertical profile properties during the fog life cycle

The analysis is first carried out on an episode that remains optically thin throughout its life cycle as the majority of fog cases sampled during the SOFOG3D campaign (8 out of 12, Table 2). Then, the contrast with fogs that underwent a transition from optically thin-to-thick is investigated with three other case studies. Finally, a generalization of the thermodynamical and microphysical properties over all fog samples of the 12 IOPs is conducted in section 4.3.

4.1 Thin fog event : IOP 13b case study

The radiation fog sampled during IOP 13b occurred during the night of February 23-24, 2020, associated with anticyclonic conditions and clear sky during the day, leading to a significant radiative cooling shortly after sunset, while wind speed remained low during this period (Fig. 8a). The fog appeared in patches around 2000 UTC and remained intermittent for two hours before visibility dropped below 1 km for a longer period between 2200 and 0000 UTC (Fig. 8a). At this point, radiative cooling stopped and the temperature stabilized at around 2.5 °C until the fog dissipated at 0018 UTC due to the advection of a 300-m thick stratus cloud at 2330 UTC, as depicted by radar reflectivity (Fig. 8c). It should be noted that this fog episode is too thin to be detected by radar, with the exception of a few isolated signals between 25 and 50 m height.

The eight profiles performed in the fog layer are displayed in Fig. 8d-e for temperature and LWC, respectively. Despite an increase of the CTH from 20 to 50 m, this fog remains optically thin throughout its life cycle (Fig. 8b). This optical thinness is associated with strong stable vertical profiles of temperature throughout the night, with γ values ranging from -34.4 to -14.1. LWC vertical profiles are characterized by high values of LWC near the ground of around 0.1-0.2 g.m^{-3} which tend to decrease with height, particularly profiles # 2 and # 3 (Fig. 8e) or to remain almost constant. Consequently, α values are also negative throughout the fog life cycle, ranging from -3.4 to -0.07, with the exception of vertical profile # 4 which reaches 1.43 due to high variability of LWC near the ground. Figure 8f illustrates the temporal evolution of γ and α during the fog life cycle and clearly shows that both parameters increase progressively with CTH from negative values close to 0, and become positive in the stratus cloud after fog dissipation. Therefore, during a fog episode that remains optically thin throughout its life cycle, stable conditions persist and appear to be associated with a vertical profile of LWC more or less decreasing with height, in contrast to the adiabatic characteristics usually observed in well-developed fogs.
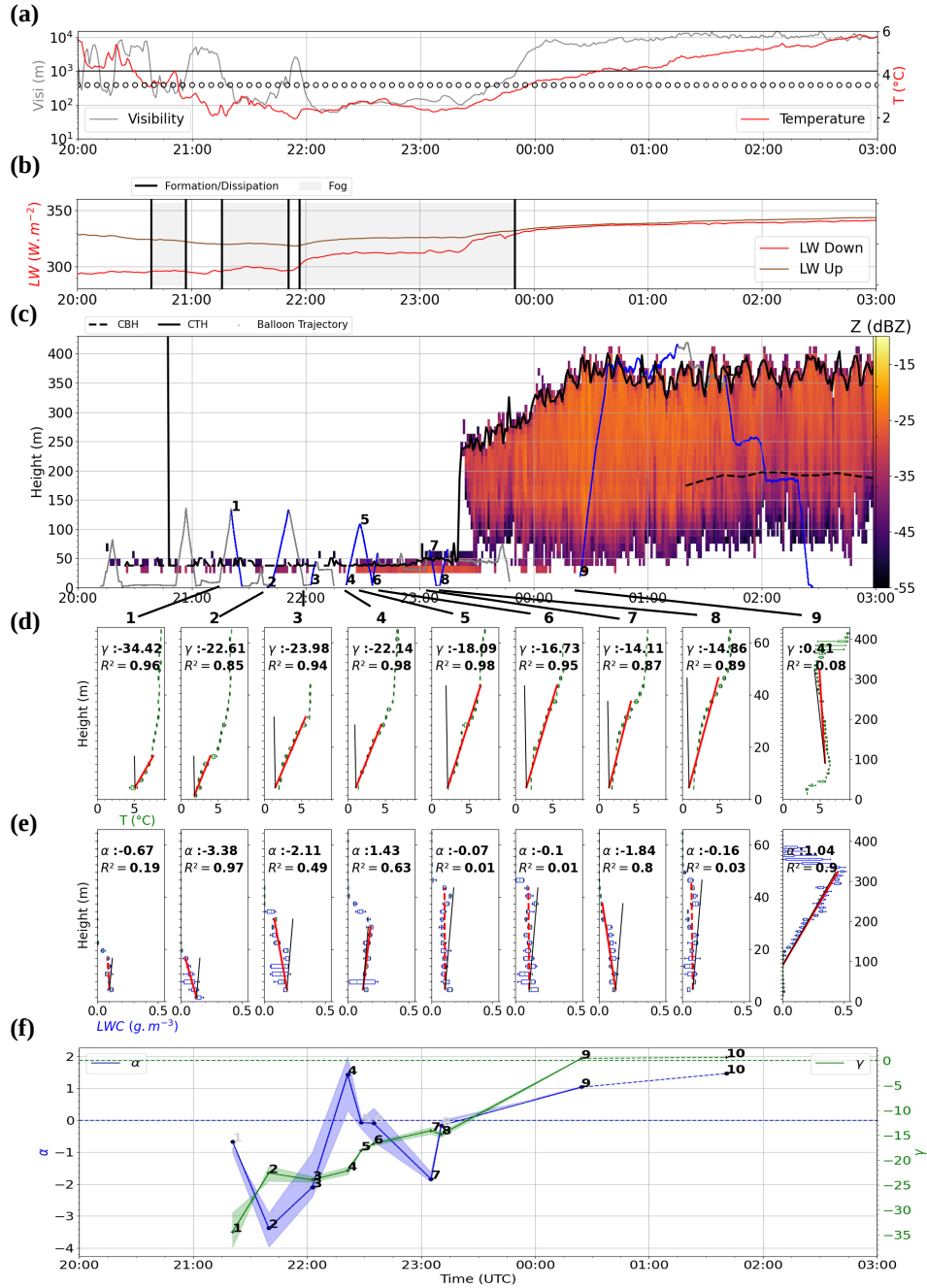
Figure 8. Temporal evolution during IOP 13b of (a) visibility, temperature at 2m and wind barbs at 10 m above ground level (empty circles, half barbs and full barbs represent wind speeds < 2.5, 5 and 10 m.s^{-1}, respectively. The orientation of the barbs gives the wind direction); (b) the upward (brown) and downward (red) longwave radiation. The gray shaded area delimitate foggy periods; (c) reflectivity and CTH derived from the BASTA cloud radar, and CBH (dashed line) from the ceilometer. The trajectory of the tethered balloon is superimposed in grey. Each selected vertical profile is highlighted in blue and labeled by its number; (d) Corresponding vertical profiles of measured temperature, with adiabaticity (red) and adiabatic lapse rate (black); (e) Corresponding vertical profiles of LWC measured by the CDP with adiabaticity (red) and adiabatic (black); (f) Temporal evolution of the adiabaticity for the selected profiles : LWC (blue line) and lapse rate (green line).

4.2 Fog events with thin-to-thick transition

4.2.1 IOP 14 case study

IOP 14 took place on the night of March 7-8, 2020, characterized by a ridge. Shortly after the last residues of the warm front had dissipated, radiative cooling set in over at the Charbonnière site associated with a low wind (Fig. 9a). A low cloud appeared on the reflectivity at around 150 m height at 2030 UTC (Fig. 9c) and lowered for 40 minutes before reaching the ground at 2120 UTC as fog formed. This cloud formation at 150 m height may be explained by the presence of a fence of trees near the Charbonnière site, i.e. in the direction of the wind, as simulated on the SIRTA site by Mazoyer et al. (2017) using Large Eddy Simulations. Due to radiative and advective processes, this fog was classified as a radiative-advective case as Dione et al. (2023) and not as a fog by stratus lowering due to its rapid descent. The fog layer remained about 100 m thick for one hour but the CTH then rapidly lowered as the wind speed aloft dropped, with the wind shifting from SW to SE direction between 2230 and 2300 UTC (see Fig. 10d of Dione et al. (2023)). The ground temperature then decreased until 2330 UTC (Fig. 9a) when the fog layer began to thicken again.

The onset of the transition phase is defined at 2330 UTC following Dione et al. (2023) and the ending times determined from the different parameters are very close within a 48-min period around 0012 UTC (Fig. 9b and Fig. 2 in section 2.3). In fact, for this case, the advection around 0030 UTC of a stratus with a base height just above the fog top height contributes to the increase of LWP above the 30 $g.m^{-2}$ threshold. The CTH derived from the radar also increased sharply above 400 m, but in situ measurements from the tethered balloon attest that it is a distinct cloud layer above the fog. The transition phase duration is therefore short for this case, less than 1 h, and included in the period determined by Dione et al. (2023) which extends to 0100 UTC. The fog began to dissipate at 0416 UTC but visibility remains around 1000-2000 m for 2 hours before it dissipated completely at 0705 UTC, shortly after sunrise, and lifted in stratus cloud that persisted until 1000 UTC.

The first three vertical profiles with CTH < 80 m reported in Fig. 9d-e were performed during the optically thin phase of the fog event. The first profile reveals low negative values of -0.62 and -1.45 for α and γ, respectively, with a reverse LWC profile which rapidly became almost constant with height for profiles # 2 and # 3 with α values close to 0. Vertical profiles # 4 and # 5, which are consecutive descent and ascent after the transition, show contrasting microphysical properties. Profile # 4 indicates a continuous increase of LWC with height throughout the fog layer, except at the fog top, consistent with the quasi-adiabatic characteristic. But the α value only reached 0.45, indicating that some dilution has occurred. The vertical profile # 5 exhibits a similar trend up to a height of 100 m, but above that, in contrast, the LWC gradually decreased up to the CTH. The temperature profiles show a significant warming between 100 and 200 m height (+ 2 °C) which explains the evaporation of liquid water in the upper part of the layer. It is likely that this warming is linked to the advection of a stratus above the fog top. In this case, the α value reached 0.65, but this represents only the lower part of the profile. The last vertical profile performed in the fog layer 5 hours later depicts also an adiabatic profile, as discussed previously (Fig. 3).

Finally, the three profiles in the stratus following fog dissipation indicate a similar trend with α and γ values between 0.56-0.79 and 0.83-1.01, respectively. Figure 9f illustrates the temporal evolution of α and γ during the fog life cycle, with the
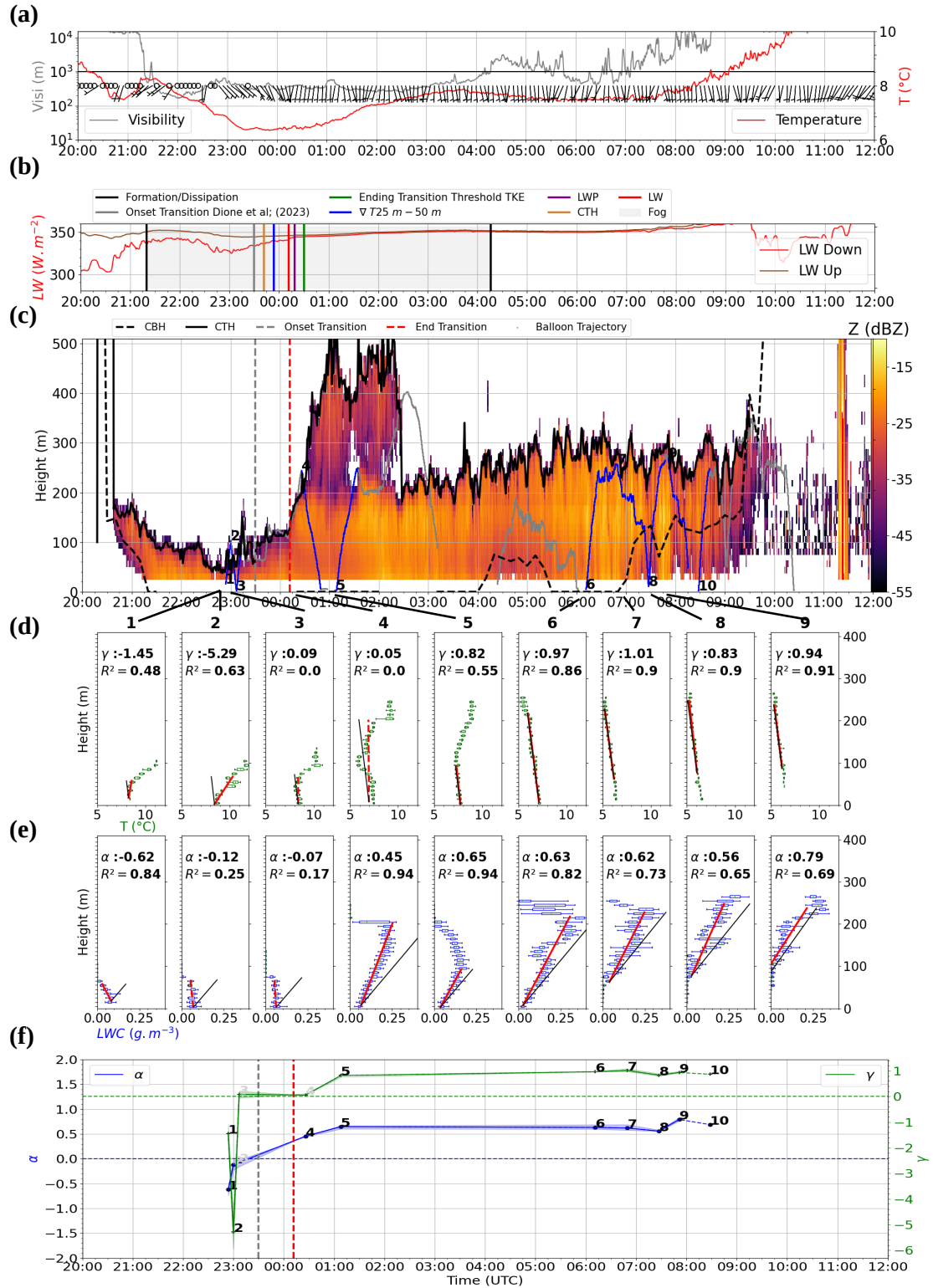
Figure 9. Same as Fig. 8 but for IOP 14. In addition b) the onset time from Dione et al. (2023) and the different ending times of the thin-to-thick fog transition are indicated by vertical lines, as in Figure 2; c) and f) the onset time is indicated by a vertical grey dashed line and the ending time derived from longwave net radiation is indicated by a vertical red dashed line.

thin-to-thick transition indicated by the dashed segment. It appears that α and γ distinctly transition from negative values, when the fog is optically thin, to positive values after the fog development.

4.2.2 IOP 11 case study

IOP 11 took place on the night of February 8-9, 2020, characterized by the establishment of a ridge after an inactive cold front had crossed the country during the day. Shortly after sunset, the sky cleared and radiative cooling set in over the Jachère and Charbonnière sites, leading to the formation of a radiative fog at 2039 UTC (Fig. 10b). This fog persisted until 0349 UTC when advection of warm air at the supersite caused the fog to lift into low stratus, which gradually dissipated until 0830 UTC.

As pointed out in section 2.3, the onset of the transition phase is determined at 2300 UTC based on Dione et al. (2023) while the end time values are very similar for the different parameters between 0030 and 0055 UTC except for LWP which took two hours more to exceed the 30 g.m^{-2} threshold (Fig. A1 in Appendix). Dione et al. (2023) considered that the transition period extended to 0230 UTC which is the longest period of their 4 cases studies.

Of the nine selected vertical profiles reported in Fig. 10d-e, three were performed during the thin phase, two during the transition, three during the thick phase and the last shortly after the fog lifted into stratus. As with IOP 14, the first three vertical profiles during the thin phase with CTH < 80 m present stable lapse rate and reverse LWC profiles with the highest values near the ground. Both α and γ values are negative but the γ values range from -2.46 and -8.97, which are higher, as for IOP 14, than those obtained during thin fog at IOP 13b, where they are systematically lower than -15. Consistently, α values range from -0.44 to -0.8, which are also generally higher than IOP 13b. Note that these higher α and γ values are associated with a thicker fog layer with CTH values from 45 m to 75 m compared with the maximum height of 50 m for IOP 13b. It is worth noting that one hour later, around 2300 UTC, the LWC # 4 profile increases slightly with height, in line with the onset of the transition period defined by Dione et al. (2023). The associated temperature profile is still globally stable, but some warming is observed between 65 and 120 m height, which could be explained by the change in wind direction. Below this, the layer between 25 and 65 m has begun to destabilize, possibly reflecting the onset of vertical motions. At the end of the transition phase (profile # 5) the entire layer was much colder and unstable. The LWC exhibited a two-layer profile with an adiabatic tendency up to 50 m height and lower values in the upper part.

Surprisingly, reverse LWC trends were observed for profiles # 6 and # 7 with $\alpha < 0$ even though the thin-to-thick transition had already ended one hour earlier. In addition, LWC values at the ground reached 0.25 g.m^{-3} which are the highest values measured on all IOPs. Note that consistently, high radar reflectivities were also observed near the ground in Fig. 10c. The corresponding lapse rates are fairly constant through the layer constrating with the stable profiles observed during the thin phase. The LWC profile becomes increasing again with a slightly positive α at profile # 8 sampled when the fog is 240 m thick, and also in stratus where α reaches 0.56 with a vertical profile of temperature that has finally destabilized with $\gamma = 1.81$. The following vertical profiles measured inside the stratus reveal the same microphysical and thermodynamical properties (not shown) as those observed in IOP 14.

Consequently, it is clear from Fig. 10f that the temporal evolution of α and γ during the fog life cycle follows the same trend as for IOP 14, from negative values when the fog is optically thin to positive values after the transition to thick fog, except for
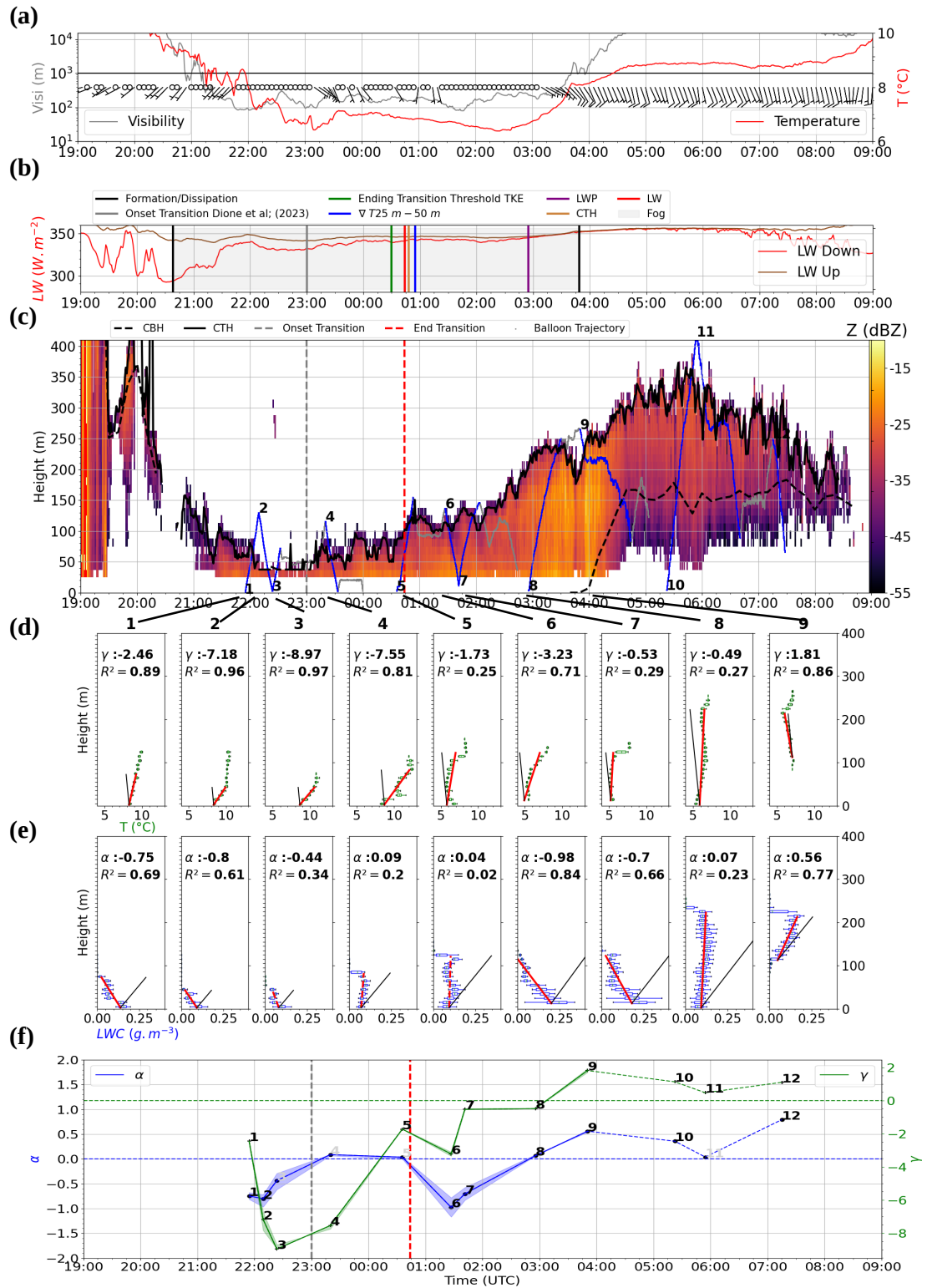
Figure 10. Same legend as Fig. 9 but for IOP 11

the sharp decrease in α for profiles # 6 and # 7, which disrupts the overall trend, due to sedimentation and collision-coalescence processes as discussed in Sec 5.

4.2.3 IOP 6 case study

IOP 6 took place during the night of January 5-6, 2020 and was characterized by anticyclonic conditions over France, associated with clear sky and negligible wind. Surface radiative cooling became established on the "Supersite" after sunset, and as the south-westerly wind began to blow, ground visibility suddenly dropped by more than 10 km in 10 minutes (Fig. 11a). This sudden fog formation at 2037 UTC is associated with the appearance of a 75 m thick liquid water layer on the BASTA reflectivity (Fig. 11c), which was also detected at different heights of the towers surrounding the "Supersite" (not shown). Fog formation was spread out over time at the various instrumented sites and was observed earlier and later for the sites located to the southwest and northeast of the domain, respectively (not shown). This suggests that a mesoscale advection coming from the west with moist maritime characteristics favoured the formation of fog in addition to radiative cooling near the ground. Therefore, we rather classify this episode as a radiative-advective fog, although Dione et al. (2023) estimated that the formation was mainly driven by radiative cooling at the surface.

As discussed in section 2.3, the transition from thin-to-thick fog ended very rapidly (50 minutes) after fog formation based on LW flux measurements. However, the vertical development of the fog layer was temporarily stopped when the wind direction shifted from southwest to southeast, and it took around 2h30 for the fog to deepen again around midnight. Consequently, the other parameters indicate a transition ending much later between 0000 for TKE and 0230 UTC for LWP, in agreement with Dione et al. (2023), who estimated that the period lasted 2 hours from midnight. Finally, the fog dissipated completely at 0928 UTC, around 1h30 after sunrise, as it lifted into a deep stratus that persisted throughout the day until it lowered and formed fog again around 1600 UTC.

Among the twenty-seven vertical profiles validated during IOP 6, nine representative profiles selected between 2152 and 0300 UTC are reported in Fig. 11 to illustrate the evolution of the microphysical and thermodynamical properties during the fog development period. In addition, the α and γ values for the last three profiles when the fog remained adiabatic, despite the decrease in thickness of around 100 m and the rise in stratus (profiles # 10 to # 12 from 0600 to 1100 UTC), are also indicated in Fig. 11f.

As a result, they all show quasi-adiabatic characteristics with positive values of α and γ, except during the period where development is stopped from 2230 to 0000 UTC. This confirms that IOP 6 became optically thick very early as indicated by LW measurements. Note that for this case, Dione et al. (2023) classified the period from 2040 to 0000 UTC as stable, considering that the transition period started at midnight, as they observed that $\alpha_{eq}(CTH)$ values remained negative with MWR LWP values $< 10\,\mathrm{g.m^{-2}}$. In contrast, the first three profiles in Fig. 11d-e show a clear increase in LWC with height associated with the quasi-adiabatic lapse rate. This suggests that other thresholds characterizing the transition with remote sensing measurements should be defined to better detect the transition when the fog life cycle is perturbed by non-local processes.

During the period corresponding to the wind rotation, the CTH dropped from 80 to 30 m in height and a large variability appears on the LWC vertical profiles. The α values decrease and become negative although the vertical profiles do not reveal
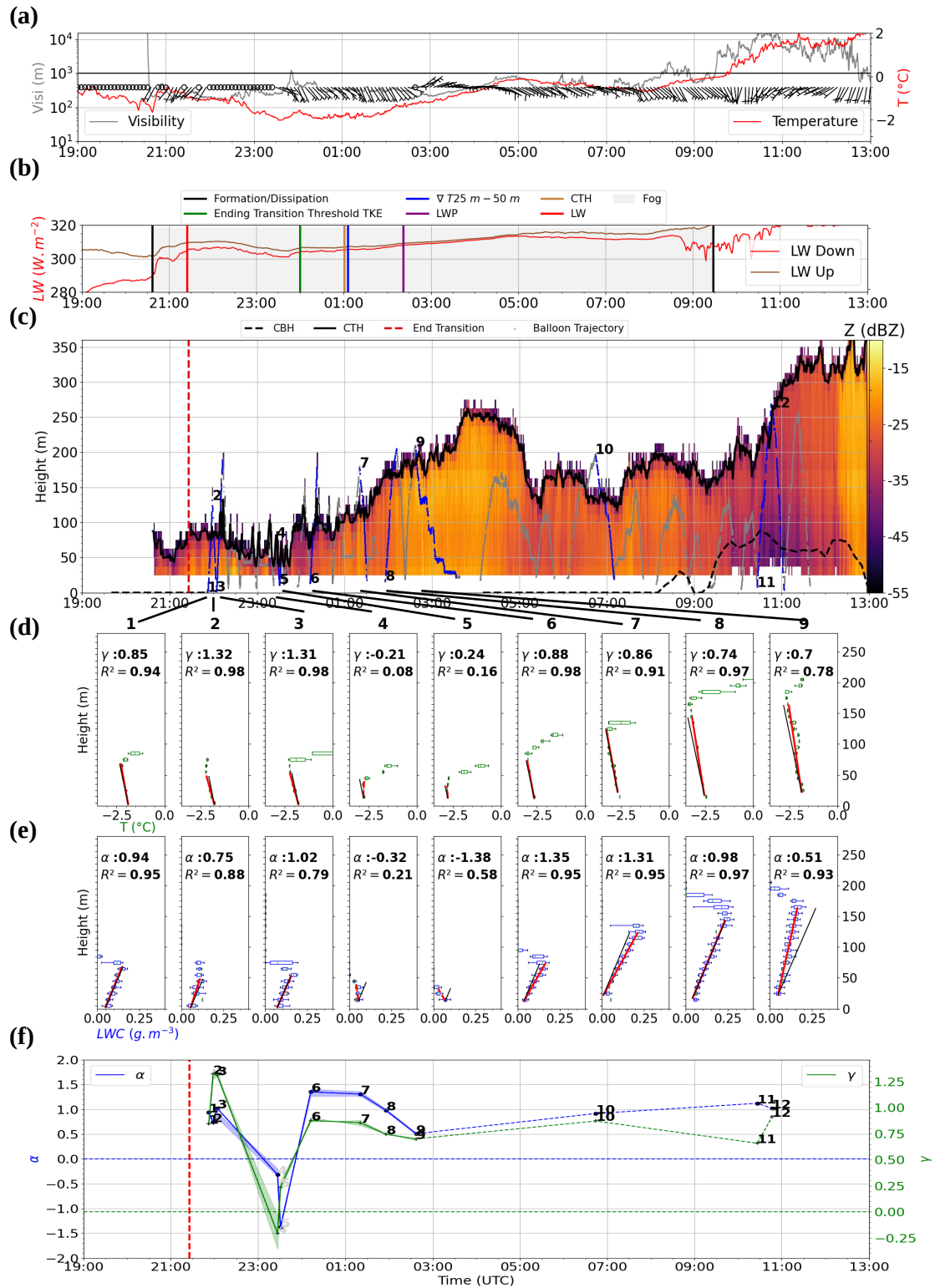
Figure 11. Same legend as Fig. 9 but for IOP 6. Visibility in (a) is issued from the Jachère site.

decreasing values with maximum values near the ground, but rather a constant LWC with height as seen on profile # 4, except for the minimum values of α = -1.38 when the fog is at its thinnest (profile # 5). During this period, the lapse rate decreased and remained almost neutral ($\gamma \approx 0$) but did not reach low negative values as in previous cases. It is likely that the layer could not return to thermally stable conditions because the time period is too short to allow coupling with the surface, despite the ground temperature lost 1 °C. From midnight, fog thickness increased again. In the same way, the LWC increased with height, and the α values are positive and range between 0.51 and 1.35 until the end of the episode, including in the stratus that followed dissipation (Fig. 11f, dotted blue line). As a result, the corresponding temperature profiles are very close to the moist adiabatic lapse rate with γ between 0.7 and 0.88.

This event therefore corroborates the fact that the profiles sampled after the thin-to-thick transition exhibit quasi-adiabatic characteristics with positive values of both α and γ, except when dynamic conditions interrupt vertical development and lead to a significant reduction in fog thickness.

4.3 Correlation between the microphysical and thermodynamical properties

The four case studies presented above have revealed a similar temporal evolution of the vertical profiles of microphysical and thermodynamical properties with contrasting patterns before and after the transition from optically thin-to-thick fog. Values of α and γ of the 140 validated profiles of the campaign are reported on Fig. 12a with empty, full circles, and diamonds, for thin and thick fogs and stratus, respectively, to highlight the contrast between the different phases.

A large majority of profiles performed during the thin phase are located in the lower left part of the graph, corresponding to negative γ and α values, while those performed in thick fog are located in the upper right part corresponding to positive or near-zero γ and α values. This trend is particularly marked for the lapse rate. For instance, $\gamma < -0.5$ for all the profiles performed in thin fog except the profile # 3 of IOP 14. Similarly, $\gamma > -0.5$ for all the profiles in thick fog except the two specific reverse LWC profiles of IOP 11. LWC profiles are a bit more scattered but $\alpha < 0$ for 74 % of the thin cases and $\alpha > 0$ for 75 % of the thick ones. The lowest α values, between -5 and -8, correspond to very stable conditions with $\gamma < -10$. These profiles performed during IOP 2b are associated with the lowest CTH values < 10 m (Fig. 12c) and also with very low LWP values < 2 g.m^{-2} (Fig. 12b). In contrast, optically thick fogs and stratus by fog lifting are associated with the highest values of LWP and CTH, as illustrated previously by IOP 6c, 13b and 14. In between, intermediate samples of γ ranging between -10 and 0 are associated with intermediate values of α around 0. These profiles are associated with CTH values reaching 50 m but not necessarily with significantly higher LWP values.

An interesting difference when comparing the thin phase of these fogs concerns the range of α and γ. For fogs that remained optically thin during their life cycle, γ ranges from -30 to -15 on average and α from -4 to 0. Whereas for those that underwent a transition to thick fog, γ ranges from -10 to 0 and α fluctuates around -1.5/-1. This would suggest that fogs that remained thin are associated with much stable conditions and stronger reverse LWC profiles. But there are only 3 thick cases sampled before the transition and more data are needed to confirm this result.

In conclusion, the analysis of the 140 profiles sampled during the experiment reveals significant differences between thin and thick fogs, with adiabaticity parameters being much lower for thin fogs (α<0, γ<-0.5) than for the thick ones and stratus
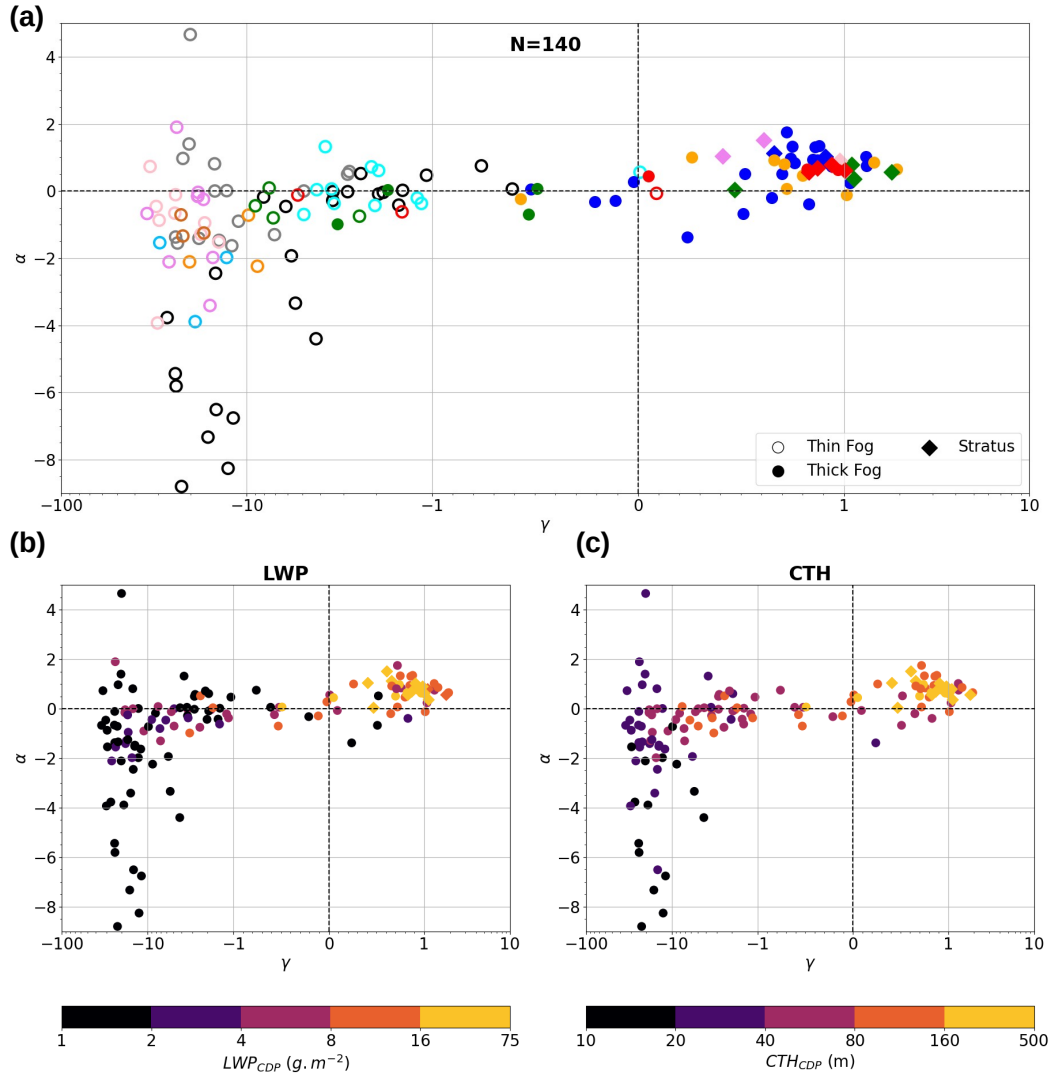
Figure 12. Adiabaticity parameter α as a function of γ in logarithmic scale, over the 12 IOPs : (a) colored with IOPs as in Fig. 4, thin and thick fog are indicated by empty dots and filled dots, respectively, (b) colored with LWP values issued from the CDP measurements, (c) colored with CTH values issued from the CDP measurements. Fog and stratus are indicated by dots and diamonds respectively.

$(\alpha>0, \gamma>-0.5)$. This confirms the temporal evolution from reverse LWC profile and stable conditions during the thin phase to quasi-adiabatic features after the transition as depicted by the 3 deepest IOPs.

5 Discussion

The CDP data collected below the tethered balloon have revealed reverse trend of LWC profile (LWC being maximal at the
675 ground and decreasing with altitude) when stable temperature conditions exist during the optically thin phase of fogs. Oliver
et al. (1978) obtained similar shape of LWC profile in advective-radiative fog by using a second-order closure model of
turbulence. But in their simulation, the fog forms in an unstable mixed layer initiated by the advection of a stable boundary
layer over a region with warmer surface temperature. Toledo et al. (2021) mentioned that such shape should exist to explain
their observations of $\alpha_{eq}^{closure} < 0$. By using cloud radar reflectivity measurements Wærsted et al. (2017) also retrieved higher
680 LWC values near the ground for a thin fog event. But to our knowledge, only two cases of LWC vertical profile decreasing with
height have been reported in the litterature. Okita (1962) measured one profile in a very thin layer < 20 m just after the fog
formation. More recently, one of the 2 profiles through the radiative fog sampled during IOP1 of the LANFEX experiment in
Boutle et al. (2018) presents also higher values at surface, with CTH < 40 m and LWP < 15 $g.m^{-2}$. Measurements presented
here then suggest that such features are ubiquitous in optically thin fogs. Because such cases correspond also to geometrically
685 thin fog layer (typically from 10 to 50 m height), the LWP is very low (typically a few $g.m^{-2}$) and these properties can hardly
be captured by current remote sensing instruments (first available gate of the cloud radar from 25 to 37.5 m height).

We therefore use these in situ data to compute adiabaticity parameters α and γ using linear regressions in order to best fit
the vertical profiles of LWC and temperature, respectively. This method allows to remove the impact of the mixing at fog top
and it is not very sensitive to significant gradients between two consecutive altitude ranges. As a result, it provides valuable
690 information to investigate departure of the general trend of the profile from the adiabatic model, and to document the evolution
during the fog life cycle, highlighting the contrast between optically thin and thick fogs. However, these calculations must
be interpreted with great caution when fog layer is thin or very thin (lower than 10 m), because it may lead to very low or
very high values of α and γ when LWC and temperature gradients are calculated on a reduced number of data. Figure C1a in
Appendix illustrates that the methods work perfectly for a sharp decrease in LWC at an altitude of 10 m, resulting in a very
695 low value of α at -8.26. But Fig. C1c-d report measurements from the first profile sampled during IOP 2a, which exhibit the
highest α value (4.66) with one of the lowest γ values (-20). This particular profile was performed at the very beginning of fog
formation, when condensation first occurred at a height of around 20 m before the surface, thus distorting the slope calculation
and giving a misleading result. This is also the case for profile # 4 of IOP 13, where slightly high values of LWC at 30 m height
combined with some low values at 10 m height lead to an α value of 1.4, whereas the profile appears to be fairly constant with
700 altitude. Thick fogs are also subject to crude approximation when profiles are not monotonic, as LWC profiles # 5 of IOP 11
and IOP 14. In such cases α values obviously can not represent the shape of the profiles.

Nevertheless, despite such uncertainty, this analysis has shown that these reverse LWC profiles sampled during the thin
phase evolve towards quasi-adiabatic features with increasing LWC values with altitude and a neutral to slightly unstable
temperature lapse rate, when the transition to optically thick fog occurs. The 3 deepest episodes presented previously provide
705 convincing elements that highlight such evolution of the vertical profiles during the fog life cycle. The number of sampled
profiles, however, is limited, and these fog life cycles were perturbed by non-local processes such as low clouds advection or

changes in wind direction, which complicate the interpretation of the observations. On the whole, however, the 140 profiles sampled during the experiment provide a robust assessment of this finding.

To determine the transition phase duration independently of the tethered balloon measurements, we used the onset time
determined by Dione et al. (2023), and defined 5 thresholds for LW flux, TKE, vertical temperature gradient, CTH and LWP
for the ending time. Optical depth which enables to discriminate between optically thin and thick fogs was also analyzed
using the CDP, but the non-continuous measurements did not allow to accurately estimate the end of the transition phase.
We found that the threshold values of 5 for optical depth and 30 g.m^{-2} for LWP proposed by Wærsted et al. (2017) are
too high for our cases and that values of 2 and 15 g.m^{-2}, respectively, are more suited. Dione et al. (2023) also found that
the adiabaticity from closure $\alpha_{eq}(CTH)$ exceeds 0.5 when LWP > 20 g.m^{-2}. In fact, in general, the fogs sampled at the
Charbonnière site during SOFOG3D have lower LWP values than previous studies at SIRTA (Wærsted et al., 2017; Toledo
et al., 2021), but similar to IOP1 of LANFEX (Boutle et al., 2018). Note that LWP measurements at Agen in the Garonne
valley during SOFOG3D were much larger, confirming that site characteristics determine fog layer properties. Note also that
while the 30 g.m^{-2} LWP threshold is too high for our dataset, the CTH threshold is adequate. This is confirmed by the new
parameterization of $\alpha_{eqCDP}^{closure}(CTH)$ which exceeds 0.5 when CTH reaches 110 m.

Transition ending time estimates from these different parameters are in agreement during IOPs 11 and 14, during which
there was a clear thin-to-thick transition (uncertainty periods of 0h25, and 0h48, respectively), but they are more dispersed
during IOPs 9a and 6c (uncertainty periods of 2h29 and 4h05, respectively) since the fog became optically thick immediately
after its formation or shortly after, respectively. It is worth noting that the evolution of the LWC profiles is consistent with these
transition period estimations, with reverse profiles before the onset of the transition evolving towards an increase of LWC with
altitude after the end of the transition. With respect to IOP 6c, the LWC profiles provide a finer scale understanding of the
fog evolution confirming that the layer is already thick very shortly after the fog onset and becoming temporarily thin as the
wind direction changes. Recently, Dione et al. (2023) proposed to additionally use the parameterization $\alpha_{eq}(CTH)$ to better
discriminate the different phases of the fog life cycle (stable, transition, adiabatic and dissipation). The resulting durations
of the transition from stable to adiabatic phase for IOP 11, 14 and 6 are 3h30, 1h30 and 2h, respectively (their Table 2).
The durations derived from our analysis are shorter, about 1h30-2h and less than 1h, for IOP 11 and 14, respectively. These
discrepancies mainly arise from their criteria that determines the end of the transition phase, namely when $\alpha_{eq}(CTH) > 0.5$
for IOP 11, but remained unclear for IOP 14. For IOP 6, the begining of the transition provided by Dione et al. (2023) is
delayed and corresponds to the second vertical development of the fog layer. Then, time series reported in Dione et al. (2023)
indicate promising evolution of $\alpha_{eq}(CTH)$ during the fog life cycle with respect to periods of thin and thick fog, but further
case studies are needed to better define the key parameter values for characterizing the transition.

We have shown that large differences exist between LWC_0 values derived from the CDP and from the visibility by the
parameterization of Gultepe et al. (2006), that contribute to the uncertainty in the calculation of $\alpha_{eq}^{closure}$. Figure 13 reveals
that LWC_0 values from CDP data are higher as α decreases for thin fogs, although there is a large dispersion, while there is a
significant reduction of LWC_0 values for $\alpha > 0$. This suggests that LWC near the ground decreases after the transition, as the
LWC profile is changing from reverse to increasing with height. This is consistent with observations of Mazoyer et al. (2022)
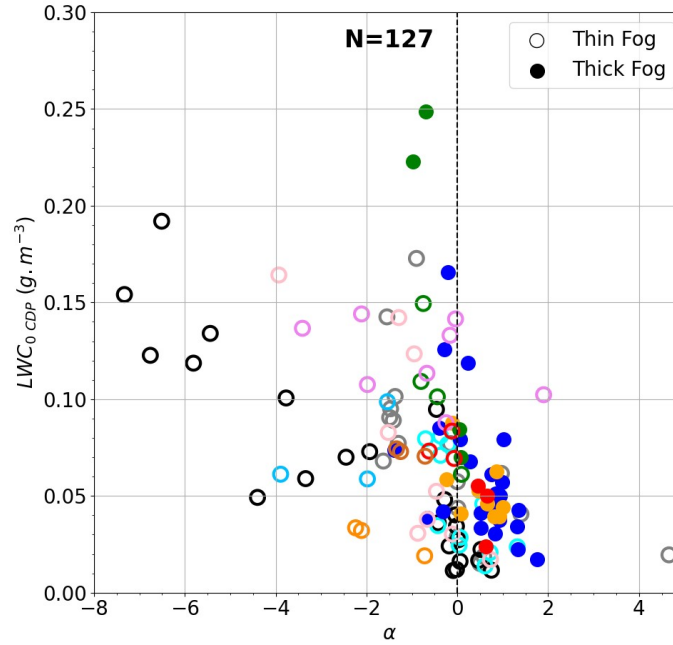
Figure 13. LWC_0 as a function of the adiabaticity α for the 12 IOPs with the same symbols as Fig. 4 and 12.

that reveal a decrease of the LWC measured near the ground during the mature phase of fogs, resulting from the evaporation due to surface warming induced by infrared radiation emitted by the fog itself.

Profiles sampled after the transition exhibit continuous increase of the LWC with height but with a large variability of the
745 adiabaticity, profiles # 6, # 7 and # 8 of IOP 6 are very close to the adiabatic, whereas profiles # 4 of IOP 14 and # 8 of IOP11 are much more diluted throughout the fog layer. We have seen that $\alpha_{eqCDP}^{closure}$ values for the few thick profiles with CTH > 150 m sampled with the CDP fluctuate around 0.4, which is below the convergence value ≈ 0.6 reported for fog conditions in Toledo et al. (2021) and Dione et al. (2023). During SOFOG3D, 13 profiles were performed in stratus cloud. They reveal that the adiabaticity is also highly variable, with profile # 9 of IOP 13b adiabatic and other very diluted such as # 8 of IOP 14 or #
750 9 of IOP 11. The mean $\alpha_{eqCDP}^{closure}$ value reaches 0.61 with 1st and 3rd quartiles of 0.48 and 0.67, respectively, and the mean α value reaches 0.76 with 1st and 3rd quartiles of 0.56 and 1.01, respectively. These statistics are in agreement with the typical adiabaticity of 0.7 observed in stratocumulus clouds from airborne measurements (Brenguier et al., 2011; Cermak and Bendix, 2011; Braun et al., 2018). This confirms that these lower adiabaticity values derived from CDP measurements result from the actual properties of the sampled fogs. Other case studies are obviously necessary to assess whether this is a general trend and
755 to better understand the processes that explain such characteristics.

As pointed out previously, the 3 LWC profiles sampled after the transition during IOP 11 depict very unexpected trend. Profile # 5 presents a two-layer structure with adiabatic increase until 50 m height and reduced values above. Such a shape has already been observed in a fog formed by stratus lowering (Fathalli et al., 2022) but it remains difficult to explain. The wind
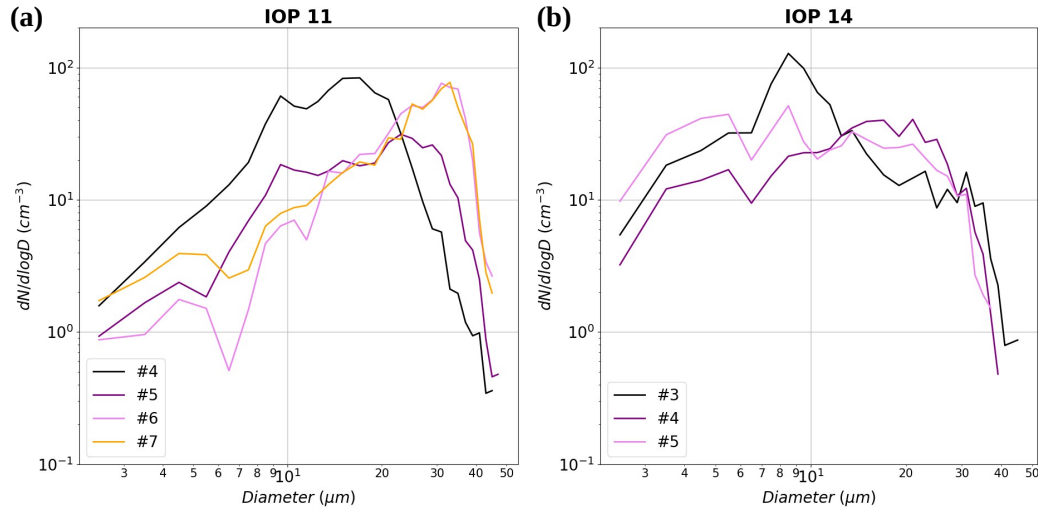
Figure 14. Droplet number size distributions measured by CDP in the 15 m thick layer above the surface for profiles (a) # 4 to # 7 from IOP 11, and (b) # 3 to # 5 from IOP 14.

and temperature profiles reported in Dione et al. (2023) (their Fig. 8d) indicate wind speed shear and strong cooling after 2300 UTC below 200 m height, suggesting that differential advection could explain this two-layer structure. Surprisingly reverse LWC trends are observed for profiles # 6 and # 7 sampled less than one hour later with the highest LWC_0 values measured near the ground (0.25 g.m^{-3}). Interestingly, these 2 LWC_0 values come out of all the samples in Fig. 6, Fig. 11a and Fig. 13. Given that, these profiles were sampled 1h30 after the transition when the fog layer was well developed, with LWP > 10 g.m^{-2} and CTH > 120 m, and the lapse rate slightly unstable: it is very unlikely that these reverse profiles result from the condensation at surface due to radiative cooling as those observed during the thin phase of radiation fogs.

Indeed, these high values of LWC_0 result from the existence of a mode of large droplets as attested by Fig. 14a, which shows the evolution of the droplet number size distributions (DSD) measured by the CDP at the surface during IOP 11. Initially centered around 15-20 μm (profile # 4 black line), the DSD broadens and shifts towards larger sizes during the transition (profile # 5 purple line). Finally, for profiles # 6 and # 7, the DSD near the ground are very similar with a mode as large as 35 μm. In contrast, for IOP 14 (Fig. 14b), the DSD before the transition exhibits a mode below 10 μm, which is further shifted to about 20 μm. Note that droplets as large as 30 μm also exist but at a much lower concentration. DSD with such mode of large droplets have been observed in many experiments as reported in Wendish et al. (1998); Gultepe et al. (2009); Niu et al. (2011); Formenti et al. (2019); Mazoyer et al. (2022); Wagh et al. (2023). Usually, they are mainly oberved in bimodal DSD and are attributed to a mass transfer from the smaller droplets into the larger ones through collision–coalescence or Ostwald ripening processes, and droplet removal through sedimentation. It is remarkable here that the DSD # 6 and # 7 of IOP 11 have a single mode and are very narrow with high concentration of large droplets. In addition, vertical profiles reveal that LWC has decreased in the upper part of the fog layer, contributing also to the reversal of the LWC trend with height. It is therefore likely

that collision–coalescence and sedimentation processes actively contributed to produce such feature by redistributing the liquid water through the fog layer from the top to the ground. A more detailed analysis of the evolution of the vertical profile of the microphysical properties is currently conducted to confirm this hypothesis and will be presented in a companion article to be submitted soon.

6 Summary and conclusions

The aim of this study was to document vertical profiles of microphysical and thermodynamic properties in fog layers from in situ measurements collected under a tethered balloon during the SOFOG3D field campaign. Droplet size distributions recorded by an adapted CDP provide 140 vertical profiles of LWC, which allow an exhaustive analysis of 8 thin fogs (thickness < 50 m) and 4 developed layers, including 3 episodes exceeding 200 m in thickness. These data reveal that reverse trend of LWC profile (LWC being maximal at the ground and decreasing with altitude) are ubiquitous in optically thin fogs, while quasi-adiabatic features with LWC values increasing with altitude are mainly observed in well-mixed optically thick fogs. We used remote sensing instruments (microwave radiometer and Doppler cloud radar) and surface measurements to determine the thin-to-thick transition ending time, based on 5 thresholds for LW flux, TKE, vertical temperature gradient, fog top height and LWP, enabling us to assess an associated interval of duration. We also used CDP data to compute optical depth on vertical profiles to provide independent measures to discriminate optically thin and thick fog periods. We found that a LWP threshold value of $15 \ \mathrm{g.m^{-2}}$ and an optical depth threshold value of 2, are more suited for the 4 thick fogs sampled at the Charbonnière site than the values of $30 \ \mathrm{g.m^{-2}}$ and 5, respectively, proposed by Wærsted et al. (2017). No tendency is observed between the time interval during which the different thresholds are reached and the duration of the transition period.

The CDP data are used to compute the equivalent fog adiabaticity from closure and compare to the value defined by Toledo et al. (2021) which is derived from remote sensing instruments, 2-m height visibility, and an one-column conceptual model of adiabatic continental fog assuming that LWC linearly increases with height. The comparison shows a large variability resulting from differences between both LWC values at ground and measurements of LWP, but their evolution as a function of the fog thickness follows the same trend, demonstrating the consistency between both methods. A new parameterization of the equivalent fog adiabaticity as a function of fog thickness was developed, on the basis of CDP observations, extending the previous parameterization for optically thin fogs. In addition, we found large negative values for thin layers, associated to low LWP values, that represent a specificity of the fog layers sampled at the Charbonnière site during the SOFOG3D experiment. In situ data are further used to investigate the actual fog adiabaticity parameters α and γ by using linear regressions to best fit the vertical profiles of LWC and temperature, respectively. We presented an analysis of 4 episodes that highlights that reverse LWC profiles, when stable temperature conditions exist during the optically thin phase of fogs, evolve towards quasi-adiabatic features with increasing LWC values with altitude, and neutral to slightly unstable temperature lapse rate, when fog becomes thick. This study reveals that non-local processes, such as low cloud advection or changes in wind direction, perturb the fog life cyle and modulate the thin-to-thick transition. On the whole, however, the 140 profiles sampled during the experiment provide a robust assessment of the vertical profile temporal evolution. We also found that LWC at ground is higher during the

thin phase, and significantly decreases as the profile is changing from reverse to increasing with height. But this trend could be balanced when collision-coalescence and sedimentation processes redistribute the LWC through the fog layer from the top to the ground.

This study provides new insights into the evolution of LWC profiles during the fog life cycle that would help constrain numerical simulations. Although this analysis is based on 140 vertical profiles, the number of samples collected during the thin-to-thick transition remains limited. More continuous observations are therefore required to examine the triggering factors of this transition and to disentangle the local and non-local processes involved in the fog life cycle. The method developed to evaluate the adiabaticity by fitting the vertical profiles of LWC allows to remove the impact of mixing at the fog top. However, the results revealed large variability among the differents cases, with some profiles highly diluted. More analysis is then needed to explain such departure from the adiabatic model in well-mixed fogs.

To take a step forward, we are currently conducting a detailed analysis of the vertical profiles of droplet size distribution measurements. Following Mazoyer et al. (2022), the main objective is to investigate the vertical and temporal evolution of the droplet size as a function of the number concentration. The vertical profile dataset is extended with constant-height sections at various altitudes within fog layers, which were performed for TKE measurements. Reflectivity and Doppler velocity along the sight of water drops, measured by the BASTA cloud radar, also provide valuable information on the dynamical and microphysical properties of the fog layer (Vishwakarma et al., 2023; Dione et al., 2023). A scanning unit was deployed around 1 km away from the vertical pointing unit of the Charbonière site, which allowed for the first time a volume sampling of a fog layer. Investigation of these data in synergy with CDP measurements would improve the three-dimensional retrieval of microphysical properties and provide new insights to better understand the key processes driving the microphysical evolution during the fog life cycle.

Appendix A: Determination of the thin-to-thick transition time

A1   IOP 11

As for IOP 14 (Fig. 2), there is consistency in the temporal determination of all the thresholds for the time of the transition phase ending (Fig. A1), which range from 0030 UTC (TKE, green line) to 0055 UTC (vertical temperature gradient, blue line), i.e. an amplitude of 25 minutes, (Table 2), the onset time being determined at 2300 UTC following Dione et al. (2023).

A2   IOP 6

A significant variability is observed in the temporal determination of the transition phase ending between all the thresholds (Fig. A2). Downward longwave radiation strongly increases at the fog formation, leading to a decrease in LW_N, reaching 5 W.m^{-2} at 2126 UTC, 49 minutes after the fog formation at 2037 UTC (Fig. A2b). At this point, a decrease in vertical temperature gradient is observed, with the fog layer closest to the ground becoming almost neutral and therefore almost reaching the vertical temperature gradient threshold (Fig. A2d). An increase in LWP and CTH is also observed at this time, with the latter close to
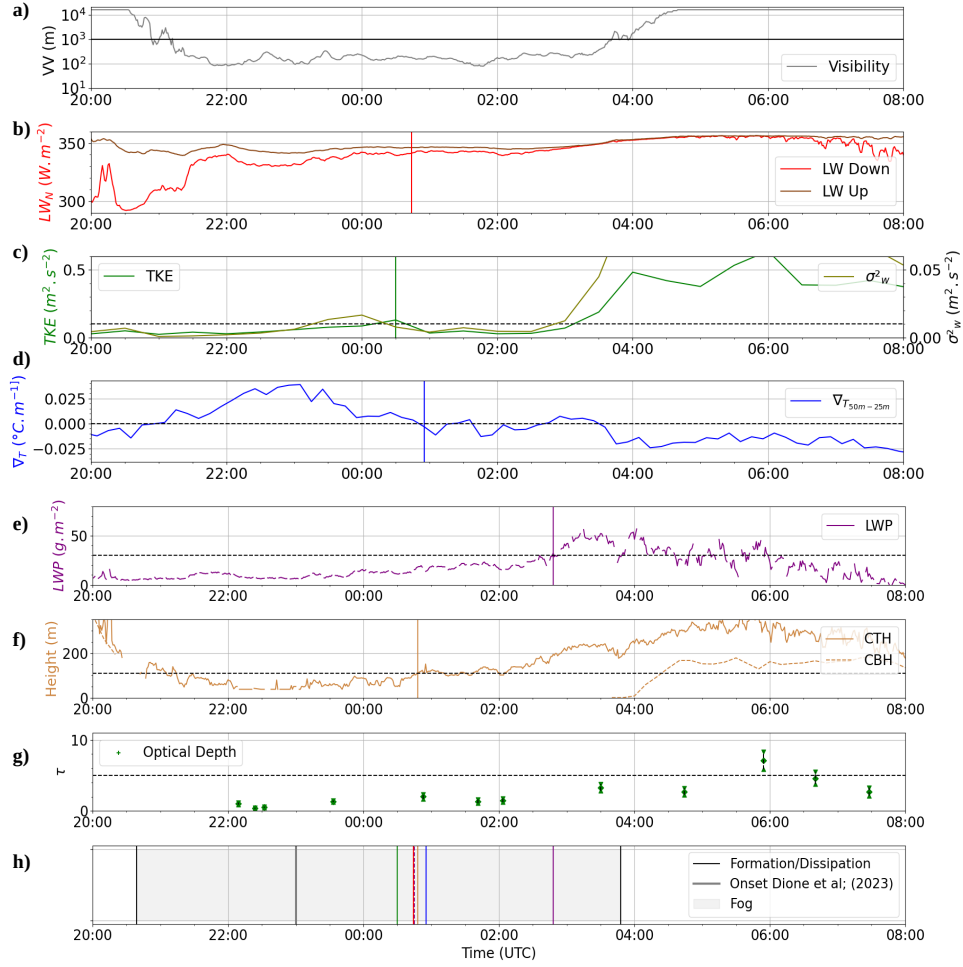
Figure A1. Same legend as Fig. 2 but for IOP 11.

the 110 m threshold (Fig. A2f). Then, all the variables diverge from their respective threshold, with the exception of LW_N. When the fog deepens vertically at around 0000 UTC (Fig. 11), TKE exceeds its threshold, while CTH, vertical temperature gradient and LWP thresholds are reached later, between 0101 and 0136 UTC. Evolution of the optical depth follows this trend, with values close to 2 shortly after fog formation and up to 6 after the vertical development at around midnight.

Appendix B: Fog equivalent adiabaticity from closure

Figure B1 illustrates the comparison between the values of $\alpha_{eq}^{closure}$ and LWP as well as CTH, using the measurements retrieved from the HATPRO radiometer and the BASTA radar respectively. The results are quite similar to that using the CDP measurements (Fig. 6). However, as in Fig. 6, some vertical profiles exhibit superadiabatic behaviour. The two profiles during
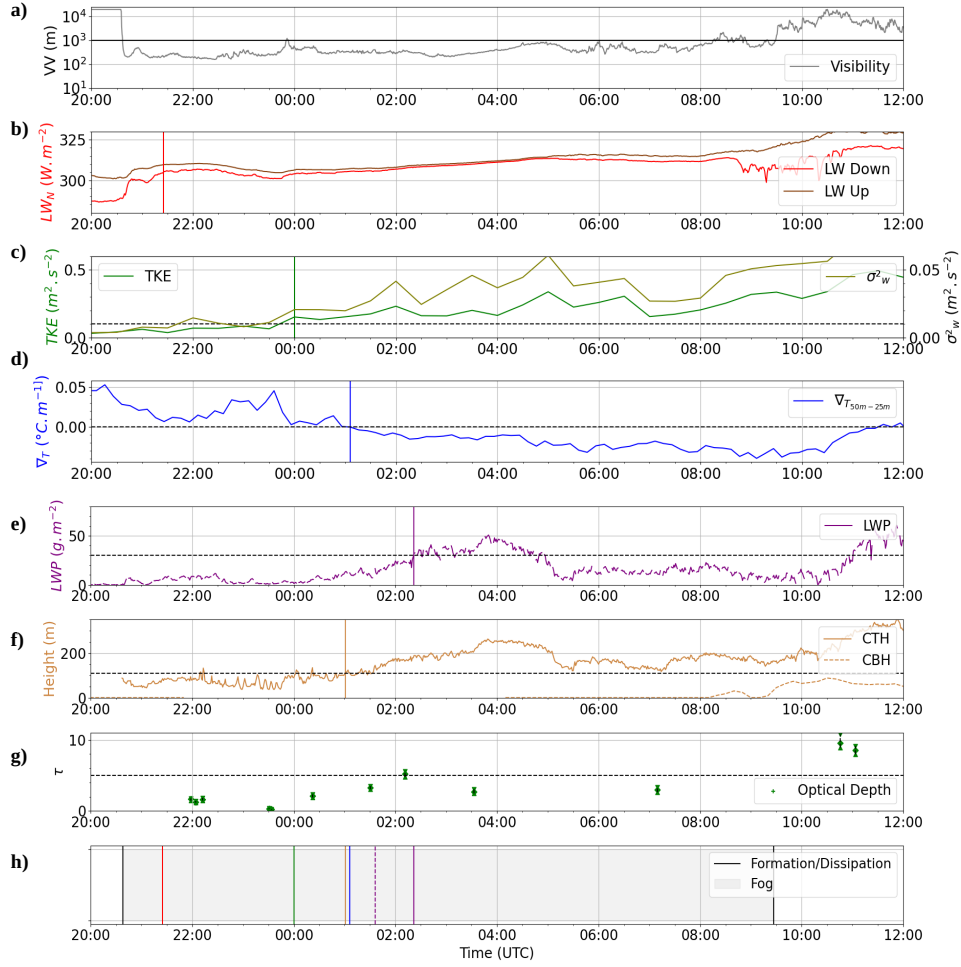
Figure A2. Same legend as Fig. 2 but for IOP 6

POI 2a (in grey) show $\alpha_{eq}^{closure}$ values greater than 1 due to low LWC_0 values, which are associated with low LWP and CTH values as well, result in a strong overestimation of $\alpha_{eq}^{closure}$. In addition, the superadiabatic vertical profiles during IOP 14 (red) and IOP 11 (green) are associated with a value of CTH just above the detection limit of the BASTA radar.

Appendix C: Vertical microphysical properties

Figure C1a,b shows the vertical profiles of temperature and LWC during IOP 2b. This IOP is characterized by three distinct fog periods, between 1924 UTC and 2110 UTC, associated with a 130 m thick fog, between 0002 UTC and 0136 with a 60 m vertically thick fog and between 0331 UTC and 0513 UTC, associated with a thin fog with a maximum CTH of 30 m. These dissipations may be explained by the presence of temporary medium and low clouds detected by the BASTA radar at around
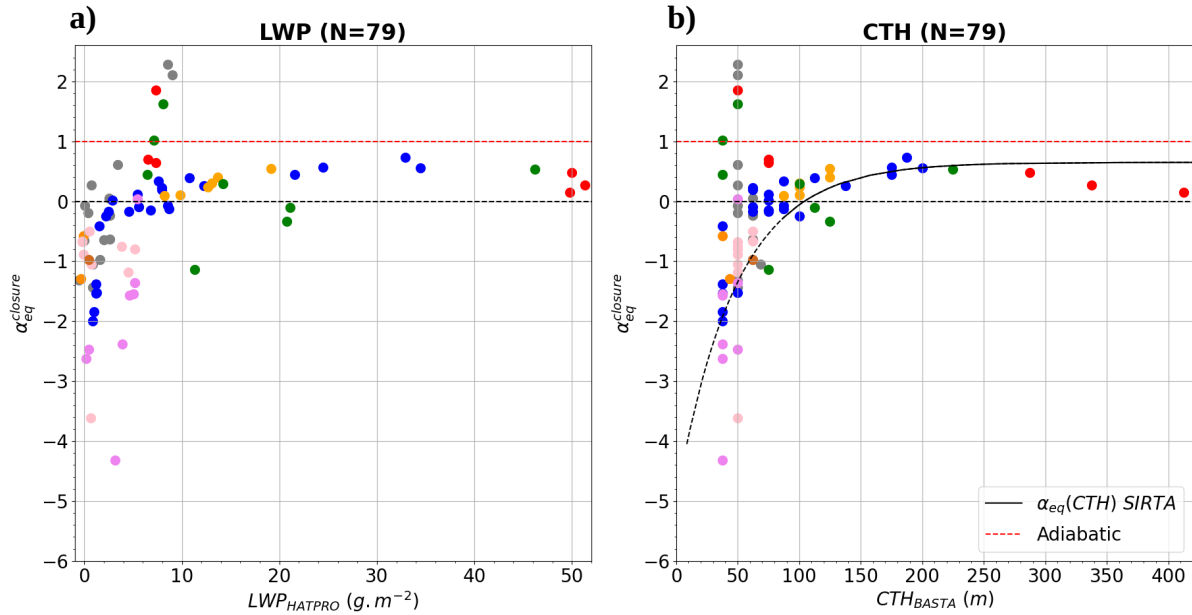
Figure B1. Same legend as Fig. 6 but using LWP and CTH derived from the HATPRO radiometer and BASTA radar, respectively.

2130 UTC and 0100 UTC, close to 3000 m and 1100 m, respectively. The two vertical profiles illustrated in Fig. C1a and C1b are representative of the last fog episode, characterized by very low values of α and γ. Figure C1c,d shows the vertical profiles
860 of temperature and LWC for the first sample during IOP 2a, which reveals a sharp increase in LWC below the fog top, related to condensation occurring at 20 m A.G.L before the surface.

Data availability. All the data used in this study are available on the French National Center for Atmospheric Data and Services (AERIS) website at the following links: https://doi.org/10.25326/XX. https://doi.org/10.25326/689 (Burnet, 2024), https://doi.org/10.25326/89 (Canut, 2020), https://doi.org/10.25326/135 (Delanoë, 2020) and https://doi.org/10.25326/207 (Martinet, 2021).

865 *Author contributions.* TC processed in situ data and performed the analysis supervised by FB and CL; Conceptualization, methodology, investigation, validation, data curation, formal analysis, visualization, writing—original draft. FB was the PI of the SOFOG3D project, designed the field campaign and led the tethered balloon operations; Project administration, resources, conceptualisation, methodology, investigation, validation, formal analysis, supervision, writing—original draft. CL was the PI of the high resolution modeling task and co-led the processes task, Conceptualization; methodology; supervision; writing—original draft. PM was the PI of the microwave radiometer
870 network; Supervision, resources, investigation, data curation. JD was the PI of the cloud radars deployment; Resources, supervision. SJ : data curation. MF : investigation, data curation.
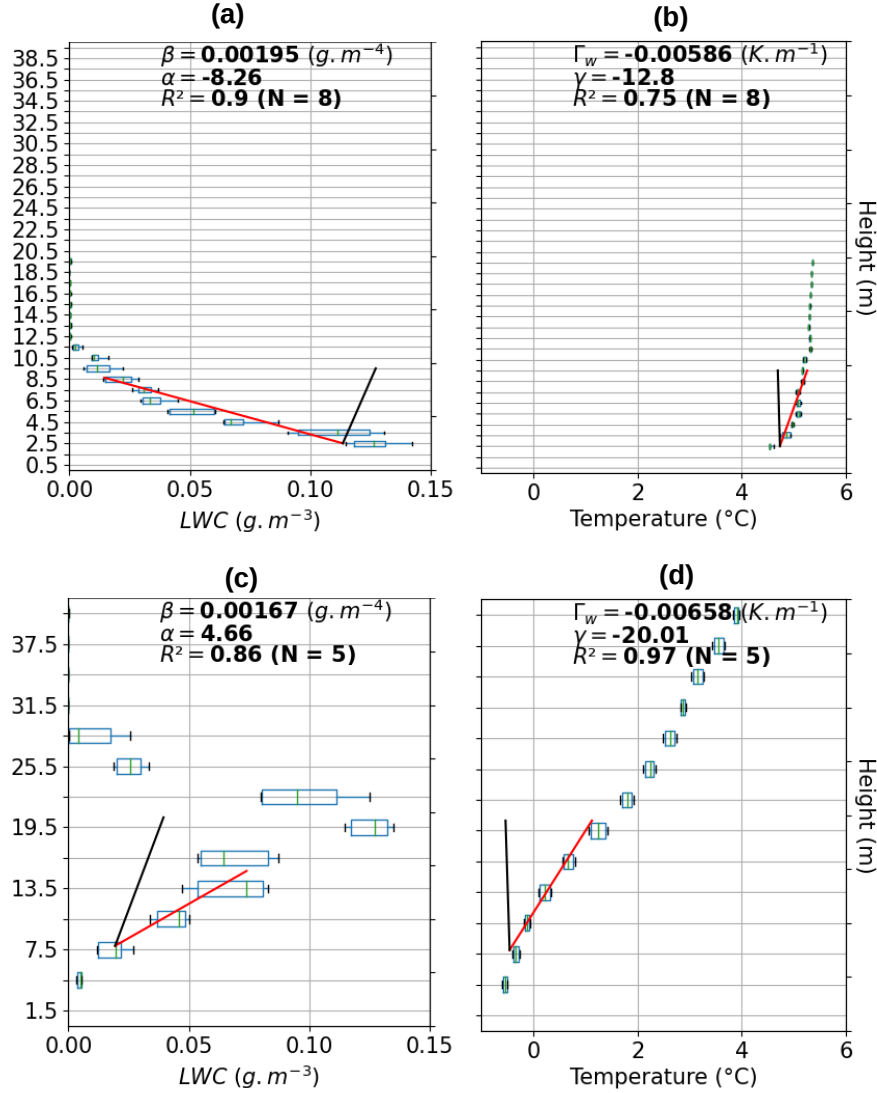
Figure C1. Vertical profile of (left) LWC (right) temperature during (a,b) the ascent between 0336 UTC and 0339 UTC of IOP 2b (c,d) the ascent between 2139 UTC and 2141 UTC of IOP 2a. Are indicated (left) the adiabatic values, the adiabaticity and the coefficient of determination of the LWC linear regression with the number of points used in brackets (right) the moist adiabatic lapse rate, the lapse rate and the coefficient of determination of the temperature linear regression with the number of points used in brackets.

Competing interests. The contact author has declared that none of the authors has any competing interests.

Disclaimer. TEXT

Acknowledgements. The SOFOG3D field campaign was supported by Météo-France and ANR through grant AAPG 2018-CE01-0004. Data
875   are managed by the French National Center for Atmospheric Data and Services (AERIS). The MWR deployment at Charbonière site was
carried out thanks to support by the Köln University. MWR data have been made available, quality controlled and processed in the frame
of CPEX-LAB (Cloud and Precipitation Exploration LABoratory, www.cpex-lab.de), a competence center within the Geoverbund ABC/J
by acting 750 support of Ulrich Löhnert, Rainer Haseneder-Lind and Arthur Kremer from the University of Cologne. This collaboration is
driven by the European COST actions ES1303 TOPROF and CA18235 PROBE. We also thank the editor and the two anonymous reviewers
880   for their constructive comments, which helped to improve the manuscript.

References

Albrecht, B. A., Fairall, C. W., Thomson, D. W., White, A. B., Snider, J. B., and Schubert, W. H.: Surface-based remote sensing of the observed and the Adiabatic liquid water content of stratocumulus clouds, Geophysical Research Letters, 17, 89–92, https://doi.org/10.1029/GL017i001p00089, 1990.

Antoine, S., Honnert, R., Seity, Y., Vié, B., Burnet, F., and Martinet, P.: Evaluation of an Improved AROME Configuration for Fog Forecasts during the SOFOG3D Campaign, Weather and Forecasting, 38, 1605 – 1620, https://doi.org/10.1175/WAF-D-22-0215.1, 2023.

Beare, R. J. and Macvean, M. K.: Resolution Sensitivity and Scaling of Large-Eddy Simulations of the Stable Boundary Layer, Boundary-Layer Meteorology, 112, 257–281, https://doi.org/10.1023/B:BOUN.0000027910.57913.4d, 2004.

Bell, A., Martinet, P., Caumont, O., Burnet, F., Delanoë, J., Jorquera, S., Seity, Y., and Unger, V.: An optimal estimation algorithm for the retrieval of fog and low cloud thermodynamic and micro-physical properties, Atmospheric Measurement Techniques, 15, 5415–5438, https://doi.org/10.5194/amt-15-5415-2022, 2022.

Bergot, T. and Guedalia, D.: Numerical Forecasting of Radiation Fog. Part I: Numerical Model and Sensitivity Tests, Monthly Weather Review, 122, 1218 – 1230, https://doi.org/10.1175/1520-0493(1994)122<1218:NFORFP>2.0.CO;2, 1994.

Bergot, T., Escobar, J., and Masson, V.: Effect of small-scale surface heterogeneities and buildings on radiation fog: Large-eddy simulation study at Paris–Charles de Gaulle airport, Quarterly Journal of the Royal Meteorological Society, 141, 285–298, https://doi.org/10.1002/qj.2358, 2015.

Betts, A. K.: Cloud Thermodynamic Models in Saturation Point Coordinates, Journal of Atmospheric Sciences, 39, 2182 – 2191, https://doi.org/10.1175/1520-0469(1982)039<2182:CTMISP>2.0.CO;2, 1982.

Bott, A.: On the influence of the physico-chemical properties of aerosols on the life cycle of radiation fogs, Boundary-Layer Meteorology, 56, 1–31, https://doi.org/10.1007/BF00119960, 1991.

Boutle, I., Price, J., Kudzotsa, I., Kokkola, H., and Romakkaniemi, S.: Aerosol–fog interaction and the transition to well-mixed radiation fog, Atmospheric Chemistry and Physics, 18, 7827–7840, https://doi.org/10.5194/acp-18-7827-2018, 2018.

Boutle, I., Angevine, W., Bao, J.-W., Bergot, T., Bhattacharya, R., Bott, A., Ducongé, L., Forbes, R., Goecke, T., Grell, E., Hill, A., Igel, A. L., Kudzotsa, I., Lac, C., Maronga, B., Romakkaniemi, S., Schmidli, J., Schwenkel, J., Steeneveld, G.-J., and Vié, B.: Demistify: a large-eddy simulation (LES) and single-column model (SCM) intercomparison of radiation fog, Atmospheric Chemistry and Physics, 22, 319–333, https://doi.org/10.5194/acp-22-319-2022, 2022.

Boutle, I. A., Finnenkoetter, A., Lock, A. P., and Wells, H.: The London Model: forecasting fog at 333 m resolution, Quarterly Journal of the Royal Meteorological Society, 142, 360–371, https://doi.org/10.1002/qj.2656, 2016.

Braun, R. A., Dadashazar, H., MacDonald, A. B., Crosbie, E., Jonsson, H. H., Woods, R. K., Flagan, R. C., Seinfeld, J. H., and Sorooshian, A.: Cloud Adiabaticity and Its Relationship to Marine Stratocumulus Characteristics Over the Northeast Pacific Ocean, Journal of Geophysical Research: Atmospheres, 123, 13,790–13,806, https://doi.org/10.1029/2018JD029287, 2018.

Brenguier, J. L.: Parameterization of the Condensation Process: A Theoretical Approach, Journal of Atmospheric Sciences, 48, 264 – 282, https://doi.org/10.1175/1520-0469(1991)048<0264:POTCPA>2.0.CO;2, 1991.

Brenguier, J.-L., Burnet, F., and Geoffroy, O.: Cloud optical thickness and liquid water path – does the k coefficient vary with droplet concentration?, Atmospheric Chemistry and Physics, 11, 9771–9786, https://doi.org/10.5194/acp-11-9771-2011, 2011.

Burnet, F.: SOFOG3D_CHARBONNIERE_CNRM_TETHERED-BALLOON-CDP-10S_L2, https://doi.org/10.25326/689, 2024.

Burnet, F., Lac, C., Martinet, P., Fourrié, N., Haeffelin, M., Delanoë, J., Price, J., Barrau, S., Canut, G., Cayez, G., Dabas, A., Denjean, C., Dupont, J.-C., Honnert, R., Mahfouf, J.-F., Montmerle, T., Roberts, G., Seity, Y., and Vié, B.: The SOuth west FOGs 3D experiment for processes study (SOFOG3D) project, in: EGU General Assembly Conference Abstracts, EGU General Assembly Conference Abstracts, p. 17836, https://doi.org/10.5194/egusphere-egu2020-17836, 2020.

Canut, G.: SOFOG3D_CHARBONNIERE_CNRM_TETHERED-BALLOON-MTO-10S_L2, https://doi.org/10.25326/89, 2020.

Canut, G., Couvreux, F., Lothon, M., Legain, D., Piguet, B., Lampert, A., Maurel, W., and Moulin, E.: Turbulence fluxes and variances measured with a sonic anemometer mounted on a tethered balloon, Atmospheric Measurement Techniques, 9, 4375–4386, https://doi.org/10.5194/amt-9-4375-2016, 2016.

Cermak, J. and Bendix, J.: Detecting ground fog from space–a microphysics-based approach, International Journal of Remote Sensing Bendix J. International Journal of Remote Sensing, 00, 3345–3371, https://doi.org/10.1080/01431161003747505, 2011.

Choularton, T. W., Fullarton, G., Latham, J., Mill, C. S., Smith, M. H., and Stromberg, I. M.: A field study of radiation fog in meppen, West Germany, Quarterly Journal of the Royal Meteorological Society, 107, 381–394, https://doi.org/10.1002/qj.49710745209, 1981.

Cuxart, J. and Jiménez, M. A.: Deep Radiation Fog in a Wide Closed Valley: Study by Numerical Modeling and Remote Sensing, Pure and Applied Geophysics, 169, 911–926, https://doi.org/10.1007/s00024-011-0365-4, 2012.

Delanoë, J.: SOFOG3D_CHARBONNIERE_LATMOS_BASTA-vertical_L2a, https://doi.org/10.25326/134, 2020.

Delanoë, J., Protat, A., Vinson, J.-P., Brett, W., Caudoux, C., Bertrand, F., du Chatelet, J. P., Hallali, R., Barthes, L., Haeffelin, M., and Dupont, J.-C.: BASTA: A 95-GHz FMCW Doppler Radar for Cloud and Fog Studies, Journal of Atmospheric and Oceanic Technology, 33, 1023 – 1038, https://doi.org/10.1175/JTECH-D-15-0104.1, 2016.

Dhangar, N. G., Lal, D. M., Ghude, S. D., Kulkarni, R., Parde, A. N., Pithani, P., Niranjan, K., Prasad, D. S. V. V. D., Jena, C., Sajjan, V. S., Prabhakaran, T., Karipot, A. K., Jenamani, R. K., Singh, S., and Rajeevan, M.: On the Conditions for Onset and Development of Fog Over New Delhi: An Observational Study from the WiFEX, Pure and Applied Geophysics, 178, 3727–3746, https://doi.org/10.1007/s00024-021-02800-4, 2021.

Dione, C., Haeffelin, M., Burnet, F., Lac, C., Canut, G., Delanoë, J., Dupont, J.-C., Jorquera, S., Martinet, P., Ribaud, J.-F., and Toledo, F.: Role of thermodynamic and turbulence processes on the fog life cycle during SOFOG3D experiment, Atmospheric Chemistry and Physics, 23, 15 711–15 731, https://doi.org/10.5194/acp-23-15711-2023, 2023.

Ducongé, L., Lac, C., Vié, B., Bergot, T., and Price, J. D.: Fog in heterogeneous environments: the relative importance of local and non-local processes on radiative-advective fog formation, Quarterly Journal of the Royal Meteorological Society, 146, 2522–2546, https://doi.org/10.1002/qj.3783, 2020.

Dupont, J. C., Haeffelin, M., Stolaki, S., and Elias, T.: Analysis of Dynamical and Thermal Processes Driving Fog and Quasi-Fog Life Cycles Using the 2010–2013 ParisFog Dataset, Pure and Applied Geophysics, 173, 1337–1358, https://doi.org/10.1007/s00024-015-1159-x, 2016.

Duynkerke, P. G.: Turbulence, Radiation and fog in Dutch Stable Boundary Layers, Boundary-Layer Meteorology, 90, 447–477, https://doi.org/10.1023/A:1026441904734, 1999.

Edwards, J. M.: Radiative Processes in the Stable Boundary Layer: Part II. The Development of the Nocturnal Boundary Layer, Boundary-Layer Meteorology, 131, 127–146, https://doi.org/10.1007/s10546-009-9363-9, 2009.

Egli, S., Maier, F., Bendix, J., and Thies, B.: Vertical distribution of microphysical properties in radiation fogs — A case study, Atmospheric Research, 151, 130–145, https://doi.org/10.1016/j.atmosres.2014.05.027, sixth International Conference on Fog, Fog Collection and Dew, 2015.

Fathalli, M., Lac, C., Burnet, F., and Vié, B.: Formation of fog due to stratus lowering: An observational and modelling case study, Quarterly Journal of the Royal Meteorological Society, 148, 2299–2324, https://doi.org/10.1002/qj.4304, 2022.

Formenti, P., D'Anna, B., Flamant, C., Mallet, M., Piketh, S. J., Schepanski, K., Waquet, F., Auriol, F., Brogniez, G., Burnet, F., Chaboureau, J.-P., Chauvigné, A., Chazette, P., Denjean, C., Desboeufs, K., Doussin, J.-F., Elguindi, N., Feuerstein, S., Gaetani, M., Giorio, C., Klopper, D., Mallet, M. D., Nabat, P., Monod, A., Solmon, F., Namwoonde, A., Chikwililwa, C., Mushi, R., Welton, E. J., and Holben, B.: The Aerosols, Radiation and Clouds in Southern Africa Field Campaign in Namibia: Overview, Illustrative Observations, and Way Forward, Bulletin of the American Meteorological Society, 100, 1277 – 1298, https://doi.org/10.1175/BAMS-D-17-0278.1, 2019.

Fuzzi, S., Castillo, R. A., Jiusto, J. E., and Lala, G. G.: Chemical composition of radiation fog water at Albany, New York, and its relationship to fog microphysics, Journal of Geophysical Research: Atmospheres, 89, 7159–7164, https://doi.org/10.1029/JD089iD05p07159, 1984.

Gerber, H.: Microphysics of Marine Stratocumulus Clouds with Two Drizzle Modes, Journal of Atmospheric Sciences, 53, 1649 – 1662, https://doi.org/10.1175/1520-0469(1996)053<1649:MOMSCW>2.0.CO;2, 1996.

Gerber, H. E.: Microstructure of a Radiation Fog, Journal of Atmospheric Sciences, 38, 454 – 458, https://doi.org/10.1175/1520-0469(1981)038<0454:MOARF>2.0.CO;2, 1981.

Gultepe, I., Müller, M. D., and Boybeyi, Z.: A New Visibility Parameterization for Warm-Fog Applications in Numerical Weather Prediction Models, Journal of Applied Meteorology and Climatology, 45, 1469 – 1480, https://doi.org/10.1175/JAM2423.1, 2006.

Gultepe, I., Tardif, R., Michaelides, S. C., Cermak, J., Bott, A., Bendix, J., Müller, M. D., Pagowski, M., Hansen, B., Ellrod, G., Jacobs, W., Toth, G., and Cober, S. G.: Fog Research: A Review of Past Achievements and Future Perspectives, Pure and Applied Geophysics, 164, 1121–1159, https://doi.org/10.1007/s00024-007-0211-x, 2007.

Gultepe, I., Pearson, G., Milbrandt, J. A., Hansen, B., Platnick, S., Taylor, P., Gordon, M., Oakley, J. P., and Cober, S. G.: The Fog Remote Sensing and Modeling Field Project, Bulletin of the American Meteorological Society, 90, 341 – 360, https://doi.org/10.1175/2008BAMS2354.1, 2009.

Guy, H., Brooks, I. M., Turner, D. D., Cox, C. J., Rowe, P. M., Shupe, M. D., Walden, V. P., and Neely III, R. R.: Observations of Fog-Aerosol Interactions Over Central Greenland, Journal of Geophysical Research: Atmospheres, 128, e2023JD038718, https://doi.org/https://doi.org/10.1029/2023JD038718, e2023JD038718 2023JD038718, 2023.

Hummel, J. R. and Kuhn, W. R.: Comparison of radiative-convective models with constant and pressure-dependent lapse rates, Tellus, 33, 254–261, https://doi.org/10.1111/j.2153-3490.1981.tb01749.x, 1981.

Koračin, D., Lewis, J., Thompson, W. T., Dorman, C. E., and Businger, J. A.: Transition of Stratus into Fog along the California Coast: Observations and Modeling, Journal of the Atmospheric Sciences, 58, 1714 – 1731, https://doi.org/10.1175/1520-0469(2001)058<1714:TOSIFA>2.0.CO;2, 2001.

Kunkel, B. A.: Parameterization of Droplet Terminal Velocity and Extinction Coefficient in Fog Models, Journal of Applied Meteorology and Climatology, 23, 34 – 41, https://doi.org/10.1175/1520-0450(1984)023<0034:PODTVA>2.0.CO;2, 1984.

Lance, S., Brock, C. A., Rogers, D., and Gordon, J. A.: Water droplet calibration of the Cloud Droplet Probe (CDP) and in-flight performance in liquid, ice and mixed-phase clouds during ARCPAC, Atmospheric Measurement Techniques, 3, 1683–1706, https://doi.org/10.5194/amt-3-1683-2010, 2010.

Maalick, Z., Kühn, T., Korhonen, H., Kokkola, H., Laaksonen, A., and Romakkaniemi, S.: Effect of aerosol concentration and absorbing aerosol on the radiation fog life cycle, Atmospheric Environment, 133, 26–33, https://doi.org/10.1016/j.atmosenv.2016.03.018, 2016.

Martinet, P.: SOFOG3D_CHARBONNIERE_CNRM_MWR-HATPRO-LWP_L2, https://doi.org/10.25326/207, 2021.

Martinet, P., Unger, V., Burnet, F., Georgis, J.-F., Hervo, M., Huet, T., Löhnert, U., Miller, E., Orlandi, E., Price, J., Schröder, M., and Thomas, G.: A dataset of temperature, humidity, and liquid water path retrievals from a network of ground-based microwave radiometers dedicated to fog investigation, Bulletin of Atmospheric Science and Technology, 3, 6, https://doi.org/10.1007/s42865-022-00049-w, 2022.

995 Mason, J.: The Physics of Radiation Fog, Journal of the Meteorological Society of Japan. Ser. II, 60, 486–499, https://doi.org/10.2151/jmsj1965.60.1_486, 1982.

Mazoyer, M., Lac, C., Thouron, O., Bergot, T., Masson, V., and Musson-Genon, L.: Large eddy simulation of radiation fog: impact of dynamics on
the fog life cycle, Atmospheric Chemistry and Physics, 17, 13 017–13 035, https://doi.org/10.5194/acp-17-13017-2017, 2017.

1000 Mazoyer, M., Burnet, F., Denjean, C., Roberts, G. C., Haeffelin, M., Dupont, J.-C., and Elias, T.: Experimental study of the aerosol impact on fog microphysics, Atmospheric Chemistry and Physics, 19, 4323–4344, https://doi.org/10.5194/acp-19-4323-2019, 2019.

Mazoyer, M., Burnet, F., and Denjean, C.: Experimental study on the evolution of droplet size distribution during the fog life cycle, Atmospheric Chemistry and Physics, 22, 11 305–11 321, https://doi.org/10.5194/acp-22-11305-2022, 2022.

Musson-Genon, L.: Numerical Simulation of a Fog Event with a One-Dimensional Boundary Layer Model, Monthly Weather Review, 115, 1005 592 – 607, https://doi.org/10.1175/1520-0493(1987)115<0592:NSOAFE>2.0.CO;2, 1987.

Müller, M. D., Masbou, M., and Bott, A.: Three-dimensional fog forecasting in complex terrain, Quarterly Journal of the Royal Meteorological Society, 136, 2189–2202, https://doi.org/https://doi.org/10.1002/qj.705, 2010.

Nakanishi, M.: Large-Eddy Simulation Of Radiation Fog, Boundary-Layer Meteorology, 94, 461–493, https://doi.org/10.1023/A:1002490423389, 2000.

1010 Niu, S. J., Liu, D. Y., Zhao, L. J., Lu, C. S., Lü, J. J., and Yang, J.: Summary of a 4-Year Fog Field Study in Northern Nanjing, Part 2: Fog Microphysics, Pure and Applied Geophysics, 169, 1137–1155, https://doi.org/10.1007/s00024-011-0344-9, 2011.

Okita, T.: Observations of the vertical structure of a stratus cloud and radiation fogs in relation to the mechanism of drizzle formation, Tellus, 14, 310–322, https://doi.org/10.3402/tellusa.v14i3.9556, 1962.

Okuda, T., Tomine, K., and Sugawara, H.: Mechanisms of Temporary Improvement and Rapid Changes in Visibility in Fogs, . 2, 88, 243–261, 1015 https://doi.org/10.2151/jmsj.2010-301, 2010.

Oliver, D. A., Lewellen, W. S., and Williamson, G. G.: The Interaction between Turbulent and Radiative Transport in the Development of Fog and Low-Level Stratus, Journal of Atmospheric Sciences, 35, 301 – 316, https://doi.org/10.1175/1520-0469(1978)035<0301:TIBTAR>2.0.CO;2, 1978.

Pagowski, M., Gultepe, I., and King, P.: Analysis and Modeling of an Extremely Dense Fog Event in Southern Ontario, Journal of Applied 1020 Meteorology, 43, 3 – 16, https://doi.org/10.1175/1520-0450(2004)043<0003:AAMOAE>2.0.CO;2, 2004.

Pinnick, R. G., Hoihjelle, D. L., Fernandez, G., Stenmark, E. B., Lindberg, J. D., Hoidale, G. B., and Jennings, S. G.: Vertical Structure in Atmospheric Fog and Haze and Its Effects on Visible and Infrared Extinction, Journal of Atmospheric Sciences, 35, 2020 – 2032, https://doi.org/10.1175/1520-0469(1978)035<2020:VSIAFA>2.0.CO;2, 1978.

Poku, C., Ross, A. N., Hill, A. A., Blyth, A. M., and Shipway, B.: Is a more physical representation of aerosol activation needed for 1025 simulations of fog?, Atmospheric Chemistry and Physics, 21, 7271–7292, https://doi.org/10.5194/acp-21-7271-2021, 2021.

Price, J.: Radiation Fog. Part I: Observations of Stability and Drop Size Distributions, Boundary-Layer Meteorology, 139, 167–191, https://doi.org/10.1007/s10546-010-9580-2, 2011.

Price, J., Porson, A., and Lock, A.: An Observational Case Study of Persistent Fog and Comparison with an Ensemble Forecast Model, Boundary-Layer Meteorology, 155, 301–327, https://doi.org/10.1007/s10546-014-9995-2, 2015.

Price, J. D.: On the Formation and Development of Radiation Fog: An Observational Study, Boundary-Layer Meteorology, 172, 167–197, https://doi.org/10.1007/s10546-019-00444-5, 2019.

Price, J. D., Lane, S., Boutle, I. A., Smith, D. K. E., Bergot, T., Lac, C., Duconge, L., McGregor, J., Kerr-Munslow, A., Pickering, M., and Clark, R.: LANFEX: A Field and Modeling Study to Improve Our Understanding and Forecasting of Radiation Fog, Bulletin of the American Meteorological Society, 99, 2061 – 2077, https://doi.org/10.1175/BAMS-D-16-0299.1, 2018.

Roach, W. T., Brown, R., Caughey, S. J., Garland, J. A., and Readings, C. J.: The physics of radiation fog: I – a field study, Quarterly Journal of the Royal Meteorological Society, 102, 313–333, https://doi.org/10.1002/qj.49710243204, 1976.

Ryznar, E.: Advection-radiation fog near lake Michigan, Atmospheric Environment (1967), 11, 427–430, https://doi.org/10.1016/0004-6981(77)90004-X, 1977.

Rémy, S. and Bergot, T.: Assessing the impact of observations on a local numerical fog prediction system, Quarterly Journal of the Royal Meteorological Society, 135, 1248–1265, https://doi.org/10.1002/qj.448, 2009.

Schwenkel, J. and Maronga, B.: Large-eddy simulation of radiation fog with comprehensive two-moment bulk microphysics: impact of different aerosol activation and condensation parameterizations, Atmospheric Chemistry and Physics, 19, 7165–7181, https://doi.org/10.5194/acp-19-7165-2019, 2019.

Steeneveld, G. J., Ronda, R. J., and Holtslag, A. A. M.: The Challenge of Forecasting the Onset and Development of Radiation Fog Using Mesoscale Atmospheric Models, Boundary-Layer Meteorology, 154, 265–289, https://doi.org/10.1007/s10546-014-9973-8, 2015.

Stolaki, S., Haeffelin, M., Lac, C., Dupont, J.-C., Elias, T., and Masson, V.: Influence of aerosols on the life cycle of a radiation fog event. A numerical and observational study, Atmospheric Research, 151, 146–161, https://doi.org/10.1016/j.atmosres.2014.04.013, sixth International Conference on Fog, Fog Collection and Dew, 2015.

Tardif, R.: The Impact of Vertical Resolution in the Explicit Numerical Forecasting of Radiation Fog: A Case Study, Pure and Applied Geophysics, 164, 1221–1240, https://doi.org/10.1007/s00024-007-0216-5, 2007.

Tardif, R. and Rasmussen, R. M.: Event-Based Climatology and Typology of Fog in the New York City Region, Journal of Applied Meteorology and Climatology, 46, 1141 – 1168, https://doi.org/10.1175/JAM2516.1, 2007.

Teixeira, J.: Simulation of fog with the ECMWF prognostic cloud scheme, Quarterly Journal of the Royal Meteorological Society, 125, 529–552, https://doi.org/10.1002/qj.49712555409, 1999.

Thornton, J., Price, J. D., Burnet, F., and Lac, C.: Contrasting the evolution of radiation fog over a heterogeneous region in southwest France during the SOFOG3D campaign, Quarterly Journal of the Royal Meteorological Society, 149, 3323–3341, https://doi.org/10.1002/qj.4558, 2023.

Toledo, F., Haeffelin, M., Wærsted, E., and Dupont, J.-C.: A new conceptual model for adiabatic fog, Atmospheric Chemistry and Physics, 21, 13 099–13 117, https://doi.org/10.5194/acp-21-13099-2021, 2021.

Turton, J. D. and Brown, R.: A comparison of a numerical model of radiation fog with detailed observations, Quarterly Journal of the Royal Meteorological Society, 113, 37–54, https://doi.org/10.1002/qj.49711347504, 1987.

Vehil, R., Monerris, J., Guedalia, D., and Sarthou, P.: Study of the radiative effects (long-wave and short-wave) within a fog layer, Atmospheric Research, 23, 179–194, https://doi.org/10.1016/0169-8095(89)90006-9, 1989.

Vishwakarma, P., Delanoë, J., Jorquera, S., Martinet, P., Burnet, F., Bell, A., and Dupont, J.-C.: Climatology of estimated liquid water content and scaling factor for warm clouds using radar–microwave radiometer synergy, Atmospheric Measurement Techniques, 16, 1211–1237, https://doi.org/10.5194/amt-16-1211-2023, 2023.

Wærsted, E. G., Haeffelin, M., Dupont, J.-C., Delanoë, J., and Dubuisson, P.: Radiation in fog: quantification of the impact on fog liquid water based on ground-based remote sensing, Atmospheric Chemistry and Physics, 17, 10 811–10 835, https://doi.org/10.5194/acp-17-10811-2017, 2017.

1070   Wagh, S., Kulkarni, R., Lonkar, P., Parde, A. N., Dhangar, N. G., Govardhan, G., Sajjan, V., Debnath, S., Gultepe, I., Rajeevan, M., and Ghude, S. D.: Development of visibility equation based on fog microphysical observations and its verification using the WRF model, Modeling Earth Systems and Environment, 9, 195–211, https://doi.org/10.1007/s40808-022-01492-6, 2023.

Wendish, M., Mertes, S., Heintzenberg, J., Wiedensohler, A., Schell, D., Wobrock, W., Frank, G., Martinsson, B., Fuzzi, S., Orsi, G., Kos, G., and Berner, A.: Drop size distribution and LWC in Po valley fog, Contributions to Atmospheric Physics, 71, 87–100, 1998.

1075   Westerhuis, S., Fuhrer, O., Cermak, J., and Eugster, W.: Identifying the key challenges for fog and low stratus forecasting in complex terrain, Quarterly Journal of the Royal Meteorological Society, 146, 3347–3367, https://doi.org/https://doi.org/10.1002/qj.3849, 2020.

Wood, R.: Drizzle in Stratiform Boundary Layer Clouds. Part I: Vertical and Horizontal Structure, Journal of the Atmospheric Sciences, 62, 3011 – 3033, https://doi.org/10.1175/JAS3529.1, 2005.

Wood, R.: Stratocumulus Clouds, Monthly Weather Review, 140, 2373 – 2423, https://doi.org/10.1175/MWR-D-11-00121.1, 2012.

1080   World Meteorological Organization: International Cloud Atlas, no. vol. 1 in International Cloud Atlas, Secretariat of the World Meteorological Organization, https://cloudatlas.wmo.int/docs/ICA_1956-Vol_I_low_res.pdf, 1956.

Yang, L., Liu, J.-W., Ren, Z.-P., Xie, S.-P., Zhang, S.-P., and Gao, S.-H.: Atmospheric Conditions for Advection-Radiation Fog Over the Western Yellow Sea, Journal of Geophysical Research: Atmospheres, 123, 5455–5468, https://doi.org/10.1029/2017JD028088, 2018.

Zhang, X., Musson-Genon, L., Dupont, E., Milliez, M., and Carissimo, B.: On the Influence of a Simple Microphysics Parametrization on

1085   Radiation Fog Modelling: A Case Study During ParisFog, Boundary-Layer Meteorology, 151, 293–315, https://doi.org/10.1007/s10546-013-9894-y, 2014.